รายงานวิจัยฉบับสมบูรณ์

โครงการเซลล์แสงอาทิตย์ชนิดสีย้อมไวแสงที่ใช้ขั้วเคาน์เตอร์จากคาร์บอนและ NiS/carbon

โดย ดร.วสันต์ ไมอักรี และคณะ

พฤษภาคม 2563

สัญญาเลขที่ MRG6180267

รายงานวิจัยฉบับสมบูรณ์

โครงการเซลล์แสงอาทิตย์ชนิดสีย้อมไวแสงที่ใช้ขั้วเคาน์เตอร์จากคาร์บอนและ NiS/carbon

คณะผู้วิจัย สังกัด

1. ดร.วสันต์ ไมอักรี มหาวิทยาลัยมหาสารคาม
2. รศ.ดร.วิทยา อมรกิจบำรุง มหาวิทยาลัยขอนแก่น

สนับสนุนโดยสำนักงานคณะกรรมการการอุดมศึกษา และสำนักงานกองทุนสนับสนุนการวิจัย

Acknowledgements

I would like to thank Thailand Research Fund (TRF), The office of the Higher Education Commission (OHEC) (MRG6180267), and Thailand Toray Science Foundation (TTSF) for research fund of this research. I would like to express my sincere gratitude to my mentor, Associate Professor Dr.Vittaya Amornkitbamrung, for the instructive support, kind teaching on experimental techniques and of publication papers, and for providing me with a better technical understanding of certain key concepts.

Wasan Maiaugree

TABLE OF CONTENTS

บทคัดย่อ

ฟิล์มคาร์บอนถูกเคลือบบนกระจกนำไฟฟ้าด้วยวิธีการอาร์คเพื่อใช้เป็นขั้วเคาน์เตอร์ในเซลล์แสงอาทิตย์ชนิดสีย้อมไวแสง คาร์บอนที่ผ่านการเผาภายใต้บรรยากาศของไนโตรเจนทำให้ประสิทธิภาพเซลล์แสงอาทิตย์เพิ่มขึ้นเนื่องจากการเพิ่มขึ้นของคุณสมบัติการเป็นตัวเร่งปฏิกิริยา เซลล์แสงอาทิตย์ที่ใช้คาร์บอนเป็นขั้นเคาน์เตอร์ให้ประสิทธิภาพเป็น 2.37% และ 2.75% เมื่อใช้ I_3^-/I^- และ T_2/T^- เป็นอิเล็กโตรไลต์ตามลำดับ ภายหลังการเผาคาร์บอนประสิทธิภาพของเซลล์แสงอาทิตย์เพิ่มขึ้นเป็น 8.04% สำหรับ I_3^-/I^- และ 4.74% สำหรับ T_2/T^- เมื่อทดสอบความเสถียรของเซลล์แสงอาทิตย์เป็นเวลา 50 วัน พบว่าในกรณีที่ใช้ไอโอไดด์อิเล็กโตรไลต์ประสิทธิภาพลดลง 20%, 25% และ 35% เมื่อใช้ขัวเคาน์เตอร์จากคาร์บอนที่ผ่านการเผา คาร์บอน และแพลตตินัม ตามลำดับ ในกรณีของไทโอเลตอิเล็กโตรไลต์นั้นประสิทธิภาพของเซลล์แสงอาทิตย์ที่ใช้คาร์บอนที่ผ่านการเผานั้นคงที่ไม่ลดลง ส่วนคาร์บอน และแพลตตินัมลดลง 26% and 39% ตามลำดับ

ฟิล์มคอมโพสิตนิเกิลซัลไฟด์ (Ni_3S_2) ถูกปลูกบนท่อนาโนคาร์บอน (MWCNTs) และเคลือบบนกระจกนำไฟฟ้าด้วยกระบวนการไฮโดรเทอร์มอลที่อุณหภูมิ 170 °C ฟิล์ม Ni_3S_2@MWCNTs ถูกใช้เป็นขั้วเคาน์เตอร์สำหรับเซลล์แสงอาทิตย์ชนิดสีย้อมไวแสง ในงานวิจัยนี้ศึกษาโครงสร้างทางกายภาพ โครงสร้างผลึก คุณสมบัติการเร่งปฏิกิริยาและการส่งผ่านอิเล็กตรอน ยิ่งไปกว่านั้นพื้นที่ผิวสัมผัสของขั้วเคาน์เตอร์ถูกวิเคราะห์เปรียบเทียบ ประสิทธิภาพการแปลงพลังงานของเซลล์แสงอาทิตย์ที่ใช้ Ni_3S_2@MWCNTs เป็นขั้วเคาน์เตอร์เพิ่มขึ้นเป็น 7.48% เมื่อเทียบกับ Ni_3S_2

คำสำคัญ: เซลล์แสงอาทิตย์ชนิดสีย้อมไวแสง, ขั้วเคาน์เตอร์, คาร์บอน, ท่อนาโนคาร์บอน, Ni_3S_2

Abstract

Carbon films were deposited by an arc evaporation method onto conductive glass and applied as counter electrodes in dye sensitized solar cells (DSSCs). Annealing the carbon films in a N_2 atmosphere contributed to the enhancement of DSSC efficiency because their electrocatalytic activities were significantly enhanced. The efficiency of solar cells with carbon films was 2.37 % and 2.75% with an I_3^-/I^- and T_2/T^- electrolyte, respectively. Whilst, that of DSSCs with annealed carbon was increased to 8.04% using I_3^-/I^- and to 4.74% for T_2/T^-. The stability of iodide-based DSSCs was not as high as that of thiolate-based units. Within 50 days, the efficiency of iodide-based DSSC with annealed carbon, Pt and as-deposited carbon dwindled by 20%, 25% and 35%, respectively. After 50 days, the efficiency of DSSCs with annealed carbon employing a disulfide/thiolate electrolyte remained constant, whilst that of DSSCs with as-evaporated carbon and Pt dropped by 26% and 39%, respectively.

Composite films nickel sulfide (Ni_3S_2) nanoparticles were grown on multiwall carbon nanotubes (MWCNTs) and in situ coated onto conducting glass substrates by the hydrothermal process at 170 °C. These Ni_3S_2@MWCNTs films were applied for counter electrodes (CEs) of dye-sensitized solar cells (DSSCs). In this work, nanostructure, crystalline structure, electrochemical activities and electron-charge transfer resistance of CEs were studied. In addition, the effective surface areas of CEs were analyzed and discussed as well. The power conversion efficiency (PCE) enhancement of up to 7.48%, compared with that of Ni_3S_2-DSSC, was demonstrated for a Ni_3S_2@MWCNTs DSSC.

Keyword: Dye-sensitized solar cells, Counter electrodes, Carbon, Carbon nanotubes, Ni_3S_2.

1. Executive Summary

1.1 Introduction to the research problem and its significance

At present, fossil fuels are the main energy resources of the world. Our primary energy needs has been fulfilled by petroleum oil, natural gas, and coals. However, these carbon-based energy resources are non-renewable and cause undesirable pollution problems. An alternative energy source that can produce promisingly-high energy density comes from a nuclear-steam turbine power plant. However, such nuclear power is notorious since the nuclear wastes are hard to be disposed and it will wreak havoc on environments particularly in the event of natural disasters. Therefore, the quest for better technologies in energy harvesting from renewable natural sources such as solar, biomass, wind and hydro power have been persisting in the field of research and development.

Straightforward utilization of the solar energy involves a direct solar - thermal conversion such as solar collector which concentrates the solar rays onto water to produce energized steam. The other promising solar related device, relies on the direct conversion of solar ray to electrical energy, is a solar cell. The ease of electrical conversion and transportation make solar cells advantageous for many applications leading to increase of the solar cell usage.

Dye-sensitized solar cell technology (DSSC) is one type of the solar cells, which has been intensively studied because of its simple structure, low fabrication costs, promising light harvesting efficiency and environmental friendliness. DSSC is considered the next generation solar cell technology. It exhibits a potential replacement for conventional silicon solar cells. The high energy conversion efficiency of dye-sensitized solar cells is accomplished through the use of a highly porous semiconductor film coated with a monolayer dye-sensitizer as the working electrode. This technology was developed by O’Regan and Grätzel in 1991. A TiO_2 photoelectrode, an electrolyte containing an I^-/I_3^- redox couple and a counter electrode are typical components of a conventional DSSC. At the counter electrode, the iodide ions are regenerated through a reduction of tri-iodide. Platinum (Pt) film is a common materials employed for a counter electrode because of its good conductivity and high electrocalytic activity. However, Pt is expensive and rare. The Pt CE costs over 40% of the whole photovoltaic cell cost regardless of its fabrication approach. Thus, other cheaper and widely available catalysts such as carbon materials (carbon black, carbon nanotube, graphite), conductive polymer, metal sulfide and metal nitride have been tested for replacing Pt. Carbon materials are good alternative materials because it is very inexpensive and simple synthesis.

In this research, we are interested in employing carbon, carbon nanotubes (CNT) and nickel sulfide (NiS) as a catalyst material, and we will use new methods for preparing the DSSC counter electrode. Fist work, we will coat carbon film on fluoride doped tin oxide glass (FTO-glass) substrate via arc evaporation technique, and used as a counter electrode. The arc evaporation is a good choice for coating carbon on conductive glass substrate and using as a counter electrode because it can make a homogeneous film, a good attachment on substrate and a good corrosion resistant. Second work, we are interested in using co-catalyst nickel sulfide - carbon nanotube composite (NiS/CNT) fabricated by a simple one-step hydrothermal process as the counter electrode of a DSSC. The performance of DSSC, counter electrode electrocatalytic activity and interface charge-transfer resistance will be studied by I-V measurement, cyclic voltammogram and electrochemical impedance spectroscopy, respectively.

1.2 Objectives

The objectives of this research are as follows:

1.2.1. To find the suitable conditions for coating carbon films on transparent conductive oxide substrates by using arc evaporation process.

1.2.2. To find the suitable conditions for preparing NiS/CNT films on FTO substrates by hydrothermal process.

1.2.3. To characterize the electrocatalytic activity of the carbon and NiS/CNT counter electrodes by the cyclic voltammetry (CV) and the electrochemical impedance spectroscopy (EIS).

1.2.4. To study the energy conversion efficiency of DSSC based on carbon and NiS/CNT counter electrodes.

1.3 Methodology

The DSSC preparation can be separated into 3 parts, there are working electrodes preparation, counter electrodes preparation and DSSCs assembly.

Working electrode preparation

Conductive glass (fluoride doped tin oxide glass, FTO) glass will be treated with $TiCl_4$ aqueous solution. The transparent and scattered TiO_2 films will be coated on the $TiCl_4$ layer by a screen printing technique using the TiO_2 paste. After that, TiO_2 films will be annealed at 500 °C, and then immerse in the dye N719 solution.

Counter electrode preparation

Fluoride-doped tin oxide glass strips (FTO-glass, 7 □/sq, Aldrich) were used as substrates for the DSSCs. Carbon films were deposited onto FTO glass using an arc evaporation method, under pressure condition at 26 mTorr and maintained at 30 A for 3 second. A graphite rod (99.96%, Ted Pella) was used as cathode and anode in arc evaporation system. The as deposited films (carbon films) were subjected to subsequent annealing in nitrogen gas at 500 °C for 5 h to produce annealed-carbon films. The sputtered Pt film was used as a reference counter electrode

Carboxyl functional groups were generated on multiwall carbon nanotubes (MWCNTs) surfaces by soaking MWCNTs in H_2SO_4 and HNO_3 acids (ratio 3:1 V/V) at room temperature. MWCNTs CEs were fabricated using the mixture of 0.2 g MWCNTs in 30 ml deionized (DI) water for hydrothermal treatment at 170 °C for 24 h. For the preparation of Ni_3S_2 CE, a well-mixed solution of 15 mM sodium hydroxide (NaOH), 12 mM thioacetamide and 10 mM nickel(II) sulfate hexahydrate ($NiSO_4(H_2O)_6$) in DI water was hydrothermally treated at 170 °C for 24 h. Similarly, a co-catalyst Ni_3S_2@MWCNTs CE was prepared by the same process and conditions in the mixture of 0.2 g of MWCNTs with 10 mM $NiSO_4(H_2O)_6$, 15 mM NaOH and 12 mM thioacetamide in 30 ml DI water. All of these obtained films were washed with DI water and dried at 85 °C in an oven.

DSSC assembly

The DSSC will be assembled using FTO/TiO_2-dye film as the working electrode and carbon films as the counter electrode. These two electrodes will be sandwiched together with a surlyn polymer film. A liquid electrolyte (organic T^-/T_2 electrolyte and inorganic I_3^-/I^- electrolyte) will be filled into the cell through a drilled hole on the counter electrode. After electrolyte filling, the drilled hole will be sealed using a surlyn polymer film covered with a piece of glass slide.

1.4. Schedule for the entire project and expected outputs

Research activity	Part 1	Part 2	Part 3	Part 4
	Month 1-6	Month 7-12	Month 13-18	Month 18-24
1. Fabrication of carbon film by using arc evaporation method.	↔			
2. Characterization of the carbon films by FE-SEM, Raman and XPS.	↔	↔		
3. Progress report (6 month)	↔			
4. Analyze of electrocatalytic activity of the carbon films by CV and EIS.	↔	↔		
5. Preparation of working electrode and assembly solar cell.		↔		
6. Measure solar cell efficiency		↔		
7. Progress report (12 month) and draft manuscript.		↔	↔	
8. Fabrication of NiS/CNT film by hydrothermal method.			↔	
9. Characterization of the NiS/CNT films by FE-SEM, XRD and XPS.			↔	↔
10. Progress report (18 month)			↔	
11. Characterization electrocatalytic activity of the NiS/CNT films by CV and EIS.			↔	↔
12. Preparation of working electrode and assembly solar cell.				↔
13. Measure solar cell efficiency				↔
14. Publication				↔
15. Completed report				↔

1.5 Publication

1.5.1 Paper title: High stability arc-evaporated carbon counter electrodes in a dye sensitized solar cell based on inorganic and organic redox mediators

Journal name: Diamond and Related Materials

Impact factor: 2.290

1.5.2 Paper title: Ni_3S_2@MWCNTs films for effective counter electrodes of dye-sensitized solar cells

Journal name: Current Applied Physics

Impact factor: 2.010

1.6 Budget details

	first-year	second-year	Total
1. Fees			
- researcher fee	156,000	156,000	312,000
2. Material Costs			
- Chemical reagents	50,000	63,000	113,000
- Electronic parts	15,000	15,000	30,000
- Computer parts (upgrade computer)	30,000	-	30,000
- Office materials	5,000	5,000	10,000
3. Operational Costs and Other expenses			
- Sample characterization expense			
(e.g. FE-SEM, TEM, XRD, XPS and Raman)	10,000	18,000	28,000
- Inclusive rate			
Electrochemical impedance spectroscopy	10,000	5,000	15,000
Cyclic voltammetry	10,000	5,000	15,000
Tafel	-	10,000	10,000
- Fare and Accommodation fee	7,000	8,000	15,000
- Copying service	2,000	-	2,000
- Report binding	-	10,000	10,000
- English academic proofreading	5,000	5,000	10,000
Total budget	**300,000**	**300,000**	**600,000**

2. Results

2.1 High stability arc-evaporated carbon counter electrodes in a dye sensitized solar cell based on inorganic and organic redox mediators

The FESEM images showing carbon deposited on FTO glass via an arc evaporation method before and after annealing in N_2 are shown in Figs. 1b and 1c, respectively. Fig 1a shows that the pyramidal grains of the fluoride-doped tin oxide film. In Fig.1b, a thin carbon film shielded the fluoride-doped tin oxide surface. The appearance of carbon morphology before and after annealing were similar.

The structural change of the carbon film subjected to thermal annealing was studied using Raman spectroscopy with 532 cm^{-1} laser excitation. Raman results are given in Fig. 2 and Table 1. It can be clearly seen that the Raman spectrum of the as-deposited film shows a characteristic broad peak that is related to an amorphous structure. The spectra consisted of disordered (D) and graphitic (G) characteristic peaks at around 1350 and 1550 cm^{-1}, respectively. Both peaks are well known as the D-peak (1350 cm^{-1}) and G-peak (1550 cm^{-1}) and are related to disorder carbon and the symmetric E_{2g} mode of graphite-like carbon, respectively [1–3]. The shoulder, located at around 1100 cm^{-1}, is related to Sp^3 bonded carbon atoms having a short range order Sp^3-carbon structure [4–6]. This Sp^3 bond may have been formed during deposition. It could have been transformed into an Sp^2 structure by the annealing process. After annealing in a N_2 atmosphere, the peak intensity of both D (1350 cm^{-1}) and G (1580 cm^{-1}) peaks became stronger. The intensity ratio of the D and G peaks (I_D/I_G) increased from 0.86 to 2.91. Furthermore, the G-peak position, which is related to the Sp^3/Sp^2 ratio, shifted to a higher wavenumber at a higher annealing temperature. This can be attributed to the transformation of an amorphous structure into a crystalline structure by a process called graphitization [5,7].

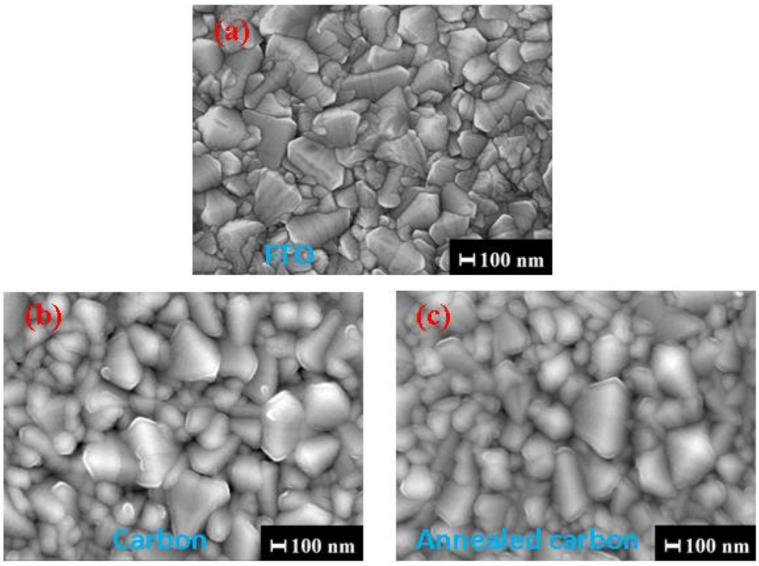

Fig. 1: FESEM images of the (a) FTO-glass, (b) and (c) are those for carbon film and annealed carbon film on FTO glass, respectively.

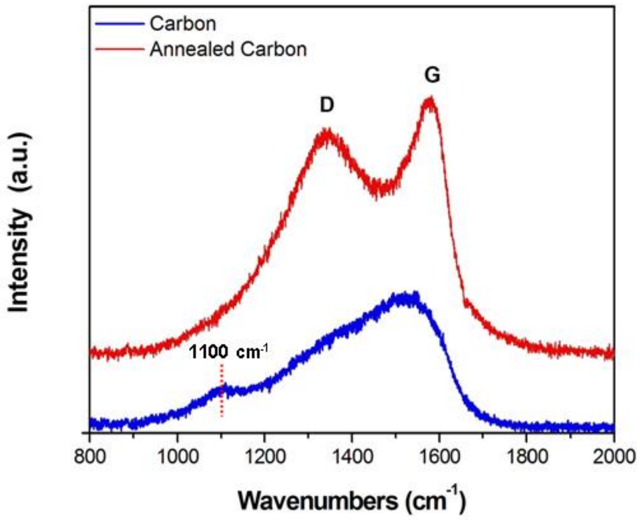

Fig. 2: Raman spectra of the carbon film and annealed carbon film on FTO glass.

Table 1: Information extracted from Raman spectra of carbon films.

Sample	Nanodiamond peak (cm^{-1})	D-peak (cm^{-1})	G-peak (cm^{-1})	FWHM of G-peak	I_D/I_G
Carbon	1100	1350	1534	182.40	0.86
Annealed carbon	-	1350	1580	116.18	2.91

The atomic bonding structure was determined from XPS. Fig. 3 shows the XPS survey spectra of the as-deposited and annealed carbon films. Both samples contained C1s and O1s. The oxygen content decreased after annealing under a low oxygen atmosphere. The approximate ratio of oxygen to carbon decreased from 0.09 to 0.03. The loss of oxygen could lead to increased film conductivity [8,9]. Figs 3b and 3c show high resolution XPS C1s spectra. The Sp^2 and Sp^3 components obtained from the deconvolution of C1s spectra were identified and are summarized in Table 2. The Sp2/Sp3 ratio increased from 2.41 to 3.73 after the film was annealed. The reason for this is due to the increase in a graphite-like phase in the film and the arrangement of Sp2 clusters [1,10]. These results agreed well with derived Raman data.

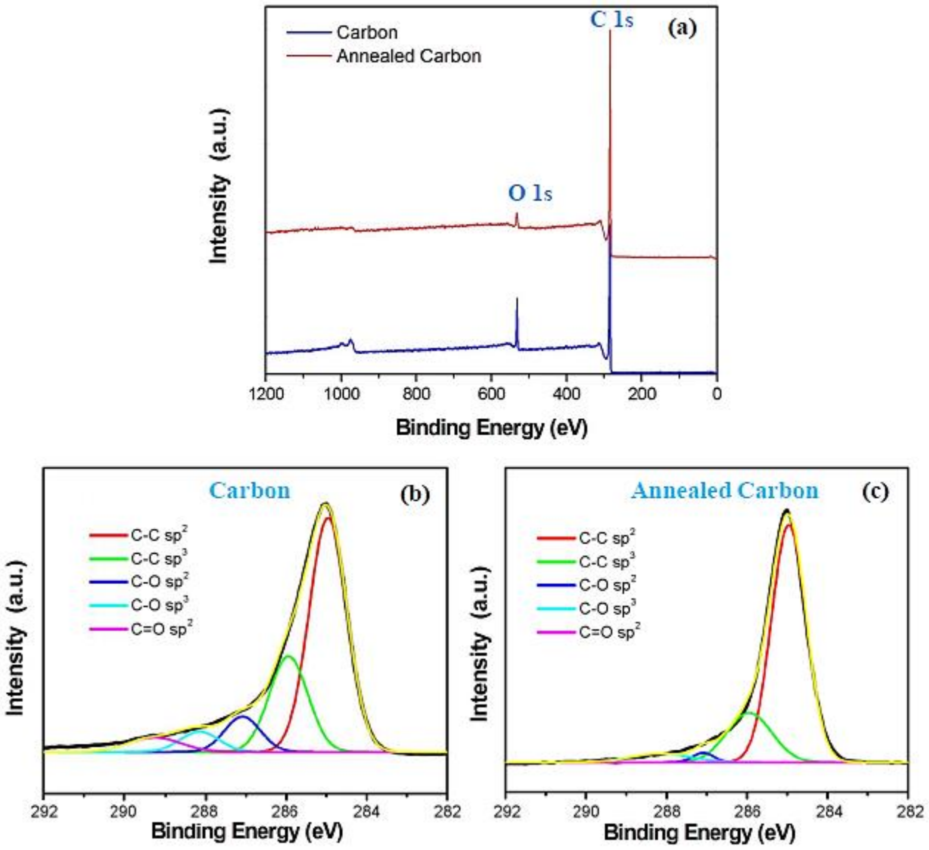

Fig. 3: (a) XPS overview spectra of carbon film and annealed carbon film, (b) and (c) high resolution XPS spectra of the C 1S region of carbon and annealed carbon film, respectively.

Table 2: XPS C1s spectra deconvolution of carbon films.

Sample	C-C sp^2 peak (cm^{-1})	C-C sp^3 peak (cm^{-1})	C-O sp^2 peak (cm^{-1})	C-O sp^3 peak (cm^{-1})	C=O sp^2 peak (cm^{-1})	sp^2/sp^3
Carbon	284.96	285.94	287.09	288.15	289.26	2.41
Annealed carbon	284.96	285.94	287.09	288.15	289.26	3.73

Cyclic voltammetry (CV) was used to analyse the electrochemical reaction of counter electrodes. The CV results of these electrodes in I_3^-/I^- and T_2/T^- are shown in Fig. 4. (a) and (b), respectively. For the iodide-based electrolyte, the Pt and annealed carbon counter electrodes presented strong oxidation peak. However, the triiodide reduction peak of annealed-carbon was weaker than that of Pt one. This implies that the electrolytic activity of annealed carbon was lower than that of Pt. The annealed carbon counter electrode exhibited a higher T^- reduction peak than that of Pt in the disulfide/thiolate electrolyte Therefore, annealed carbon exhibited better electrocatalytic activity for reducing disulfide. The reason for this is that Pt was affected by sulfur adsorption on its surface. Pt-S bonds blocked the effective surface area whilst carbon did not behave in this manner. The potential differences between the oxidation and reduction reaction (ΔE_P) was inversely related to the electron transfer rate constant (k_S). A smaller value of ΔE_P corresponded to a higher k_S [11–14]. In the triiodide/iodide system, ΔE_p of Pt was 22 mV, whilst that of annealed carbon was 50 mV. The electron transfer rate of the annealed carbon could have been smaller than that of Pt. Nonetheless, for the disulfide/thiolate system, ΔE_p of annealed carbon (62 mV) was larger than that of Pt (75 mV), implying that the electron transfer rate of annealed carbon was higher than that of Pt. This confirmed that annealing carbon drastically altered the electrochemical characteristics of the as-deposited carbon as the reduction peak was barely evidenced.

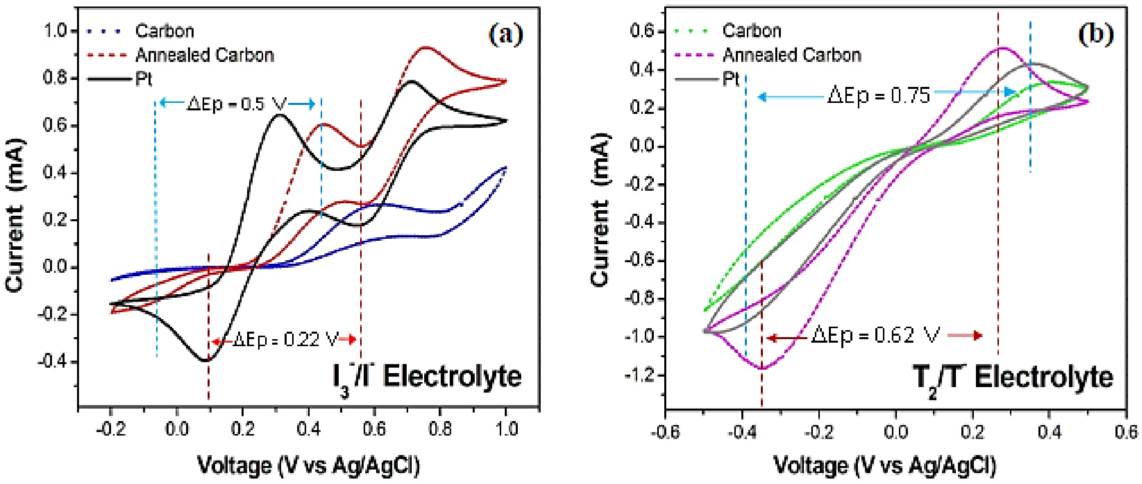

Fig. 4: CV curves of all counter electrodes based on (a) I_3^-/I^- and (b) T_2/T^- electrolytes.

Symmetrical counter electrode cells were fabricated for electrochemical impedance spectroscopy (EIS) characterization to analyse the series resistance (R_s), charge transfer resistance (R_{ct}), capacitance (C_μ) and Nernst diffusion (Z_d). The EIS spectra and analysed parameters are shown in Fig. 5 and Table 3, respectively. Simple equivalent circuits, as shown in Fig. 6, were used. Presumably, there are two R_{ct} and one R_{ct} for as-deposited carbon and annealed carbon, respectively. For simplicity, R_{ct} is the total charge transfer resistance ($R_{ct1}+R_{ct2}$) for the carbon sample. From Table 3, the R_s value for annealed carbon was lower than that of the as-deposited carbon for both electrolytes. This was due to the increased content of a graphitic phase. However, the R_s value for both carbon samples was still higher than that of Pt. The EIS spectra for the as-deposited carbon, as shown in Fig. 5, is comprised of two semi-circular arcs. The smaller arc is related to the smaller value of R_{ct}. This parameter should be related to the interfacial resistance between the electrolyte and conductive phase, such as the crystalline graphitic phase that was vaporized from the graphite rod and deposited on the samples. It is notable that there should be a small amount of a graphite phase, since its G-peak was not clear. The other arc, with a larger R_{ct} (R_{ct2}) in the as-deposited carbon, can be attributed to the interfacial resistance between the electrolyte and the less conductive phases, such as amorphous carbon and nanodiamond, whose D and G peaks also appeared in the Raman spectra. For the annealed sample, only one semicircular arc was clearly observed. This is because the amorphous phase and nanodiamond could be transformed to a more graphitic phase. The R_{ct} of annealed carbon (75.5 Ω•cm^2) and as-deposited carbon (493.8 Ω•cm^2) were higher than that of Pt (5.66 Ω•cm^2) using the ioidide electrolyte. Nevertheless, for the disulfide/thiolate electrolyte, the R_{ct} of annealed carbon (20.25 Ω•cm^2) was less than that of Pt (38.89 Ω•cm^2) and as-deposited carbon (366.20 Ω•cm^2). This implied that the annealed carbon counter electrodes had a higher electrocatalytic activity than that of a typical Pt counter electrode for the disulfide/thiolate electrolyte, whereas that of Pt was better than that for the anneal carbon in the I_3^-/I^- electrolyte. The trend of impedance results corresponds well with the CV analysis.

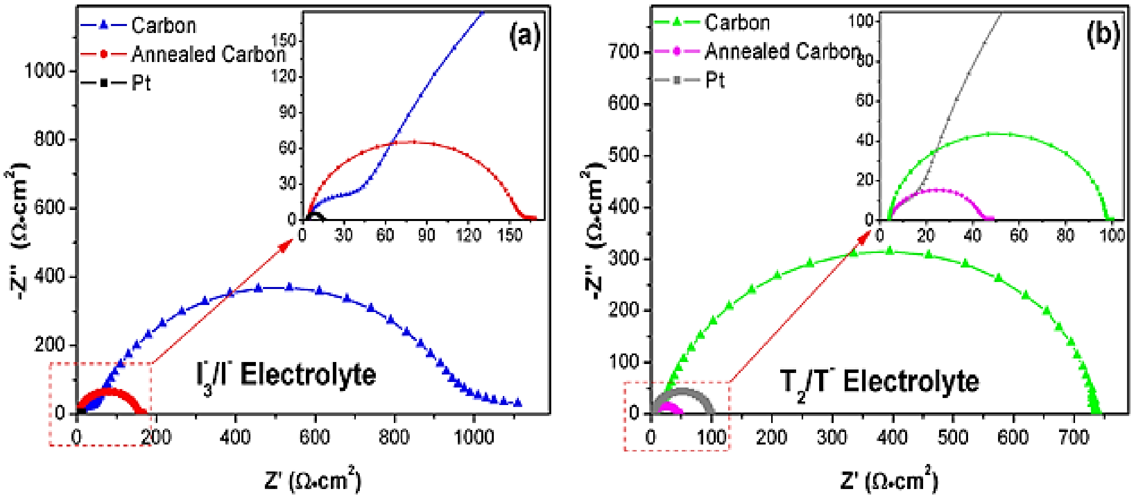

Fig. 5: Nyquist plots for symmetric cells with two identical counter electrodes of the carbon and annealed carbon based on (a) I_3^-/I^- and (b) T_2/T^- electrolytes.

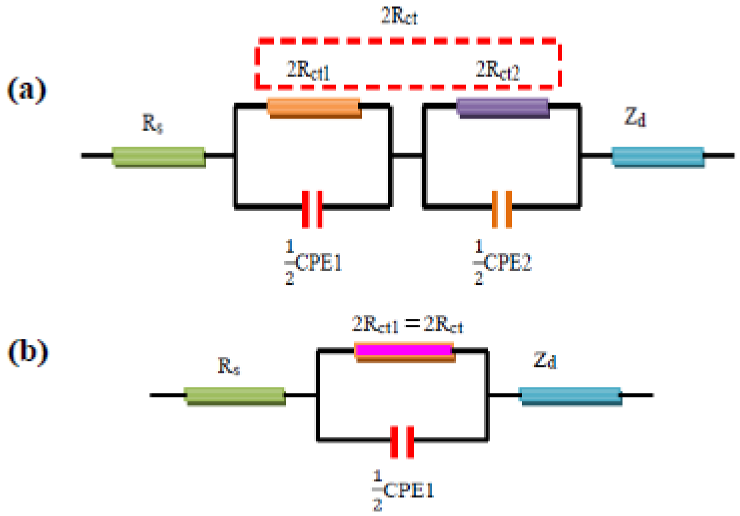

Fig. 6: Equivalent circuit for symmetrical counter electrode of (a) carbon and (b) annealed carbon films.

Table 3: Summary of the R_s, R_{ct}, J_{sc}, V_{oc}, FF and η values.

Counter electrode	**Electrolyte**	**EIS**			
		R_s (Ω.cm^2)	**R_{ct1} (Ω.cm^2)**	**R_{ct2} (Ω.cm^2)**	**R_{ct} (R_{ct1}+ R_{ct2}) (Ω.cm^2)**
Carbon	I_3^-/I^-	4.45	16.30	477.5	493.8
Annealed- Carbon	I_3^-/I^-	4.01	75.50	-	75.50
Pt	I_3^-/I^-	3.05	5.66	-	5.66
Carbon	T_2/T^-	4.36	6.20	360.0	366.20
Annealed- Carbon	T_2/T^-	3.91	20.25	-	20.25
Pt	T_2/T^-	3.89	46.65	-	38.89

Counter electrode	**Electrolyte**	**DSSCs**				
		J_{sc} (mA/cm^2)	**V_{oc} (V)**	**FF**	**η (%)**	***Average* η (%)**
Carbon	I_3^-/I^-	17.72	0.75	0.16	2.11	2.01 ± 0.44
Annealed- Carbon	I_3^-/I^-	18.56	0.74	0.64	8.74	8.36 ± 0.34
Pt	I_3^-/I^-	18.57	0.77	0.62	8.80	8.48 ± 0.30
Carbon	T_2/T^-	13.40	0.63	0.32	2.75	2.69 ± 0.05
Annealed- Carbon	T_2/T^-	16.53	0.64	0.45	4.74	4.52 ± 0.23
Pt	T_2/T^-	13.51	0.62	0.50	4.18	3.98 ± 0.17

The electrocatalytic activity of the counter electrodes can be verified from Tafel polarization of symmetrical cells (Fig. 7). The charge transfer resistance ($R_{ct,\ Tafel}$) is an inverse variable with the exchange current density (J_0) from Tafel polarization following equation (1).

$$J_0 = \frac{RT}{nFR_{ct,Tafel}} \tag{1}$$

where R is the gas constant, F is the Faraday constant, T is the absolute temperature and n is the number of electrons participating in the reaction. The trend of $R_{ct,Tafel}$ must follow that of R_{ct} derived from the EIS analysis ($R_{ct,EIS}$) [37]. The $R_{ct,EIS}$ was observed to be the lowest for the iodide-based electrolyte in Pt, resulting in the highest J_0 of Pt. This was confirmed from Tafel polarization. Pt had the highest J_0 value. Moreover, annealed carbon had a higher J_0 value than that of carbon, so the CEs electrocatalytic activity followed the relationship: Pt > annealed carbon > carbon. Using the thiolate-based electrolyte, the highest J_0 was observed for annealed carbon, which was higher than that of Pt. Therefore, the electrocatalytic activity of annealed carbon was higher than that of Pt, in this case.

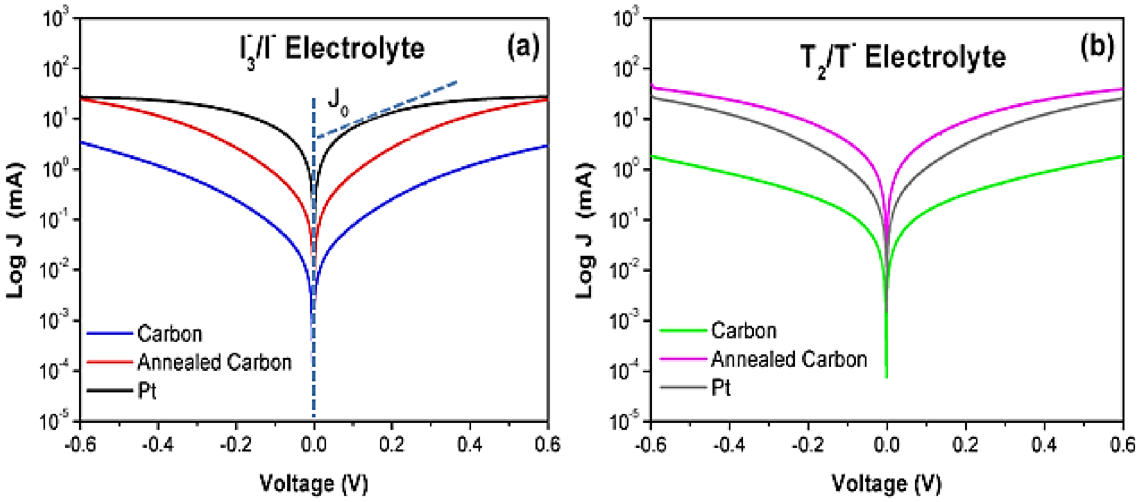

Fig. 7: Tafel curves of the carbon and annealed carbon based on (a) I_3^-/I^- and (b) T_2/T^- electrolytes.

J-V curves are shown in Fig. 8 (a) and (b) for all Pt and carbon DSSCs with triiodide/iodide based and disulfide/thiolate electrolytes, respectively. The related photovoltaic parameters are listed in Table 3. In the case of the iodide electrolyte, the short-circuit current density (**J_{sc}**) value of the as-deposited carbon, annealed carbon and Pt were 17.72, 18.56 and 18.57 mA/cm^2, respectively. The open-circuit voltage (**V_{oc}**) value of all samples was around 0.74 - 0.77 V. Fill factor of annealed carbon (0.64) was close to that of Pt (0.62) and both were higher than that of as-deposited carbon (0.16). The solar efficiency of the DSSC using annealed carbon (8.74%) was close to that of Pt (8.80%) and higher than that of as-deposited carbon (2.11%).

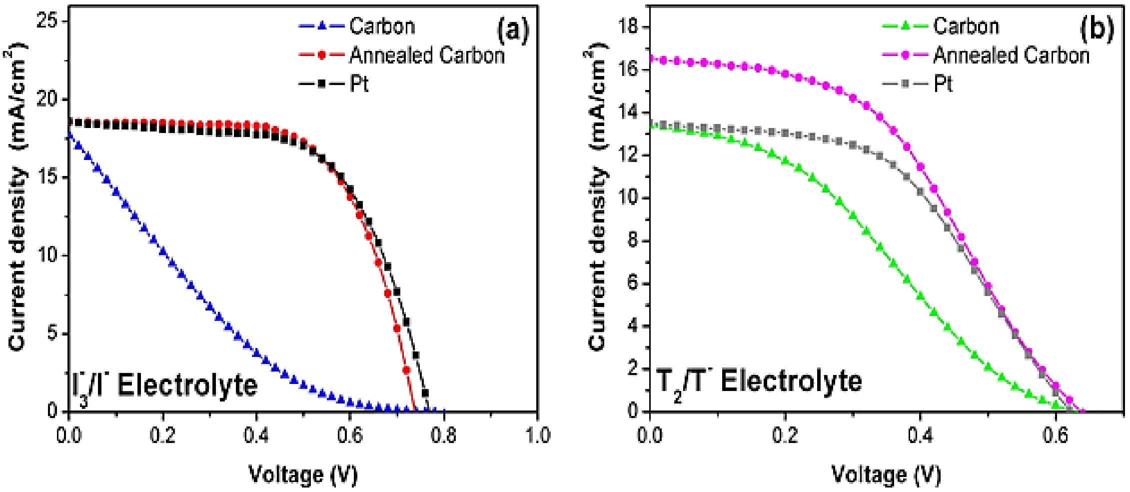

Fig. 8: J–V curves for the DSSCs with the carbon and annealed carbon based on (a) I_3^-/I^- and (b) T_2/T^- electrolytes.

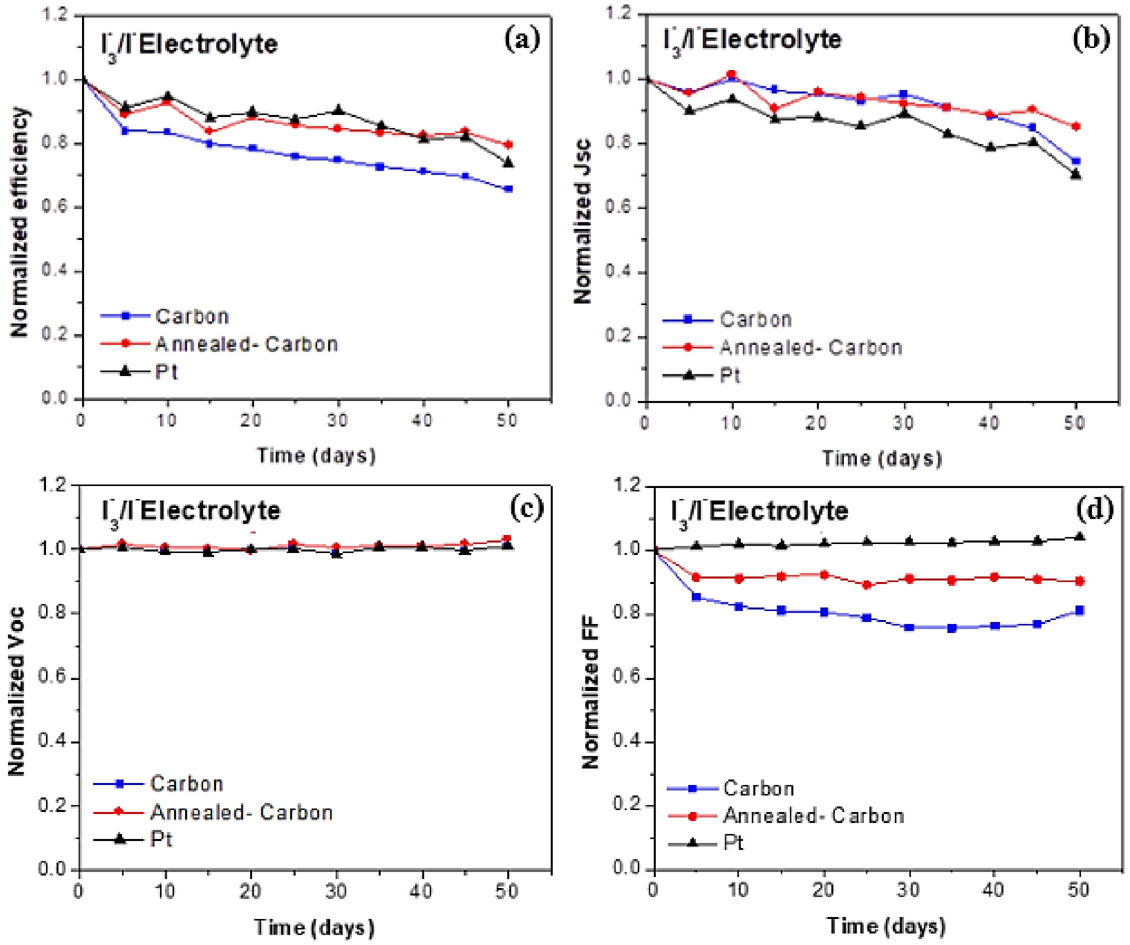

Fig. 9: Normalized (a) efficiency, (b) J_{sc}, (c) V_{oc} and (d) Fill factor of the DSSCs based on I_3^-/I^- electrolyte.

For the T_2/T^- electrolyte, the highest efficiency was achieved for the annealed carbon DSSC (4.74%), compared to those of Pt DSSC (4.18%) and as-deposited carbon DSSC (2.75%). This can be explained by the enhancement of J_{sc} (16.53 mA/cm^2) in the annealed carbon compared to those of Pt (13.51 mA/cm^2) and as-deposited carbon (13.40 mA/cm^2). The V_{oc} for all sample were close to 0.63 V, which was lower than that of the triiodide/iodide system. Moreover, the J_{sc} of anneal carbon in the I_3^-/I^- system was higher than that of the T_2/T^- system. The reduction in V_{oc} and J_{sc} values could result in the reduction of solar efficiency. The FF of annealed carbon (0.45) was close to that of Pt (0.50), but both were higher than that of the as-deposited carbon (0.32). The increase in the J_{sc} and FF values came from the graphitized constituents, resulting in the higher electrocatalytic activity and low charge transfer resistance. This was confirmed by the CV and EIS results and was similar to that of iodide. These results show the promising potential use of annealed arc-carbon as an alternative counter electrode to replace expensive Pt electrode. Fig. 9 and Fig. 10 show the stability tests of DSSC cells. For both electrolytes, the V_{oc} values were quite stable. Comparing FF values of all electrodes in the triiodide electrolyte, it was found that the FF value for Pt infinitesimally changed, whereas those of carbon types were reduced by ~10% for the annealed carbon and ~20% for the as-deposited carbon after the 50th day. However, in the case of the T_2/T^- electrolyte, the reduction of FF values of annealed carbon (~10 %) was smaller than those of Pt (~30%) and as-deposited carbon (~30%). In a triiodide/iodide electrolyte, annealed carbon showed a smaller decrease in J_{sc} (10%) than those of other electrodes, ~30% for Pt and ~25% for as-deposited carbon. For the T_2/T^- electrolyte, the J_{sc} values of annealed carbon and Pt changed little, whereas the J_{sc} of as-deposited carbon decreased (10%). The efficiency of all electrodes using an I_3^-/I^- electrolyte had a tendency to decrease with time, resulting in a 20%, 25% and 35% reduction in efficiency for annealed carbon, Pt and as-deposited carbon, respectively. The stability of the annealed carbon film was similar to that of Pt because it is possible for the iodide to be adsorbed on to the surface of carbon, reducing the electrocatalytic activity of the counter electrode, while Pt could be vulnerable to iodide corrosion. For the disulfide/thiolate electrolyte, the annealed carbon was stable, so its solar efficiency was infinitesimally affected, whilst Pt and as-deposited carbon showed decreases in solar efficiency of 26% and 39%, respectively. The explanation for this reduction is the formation of Pt-S bonds for disulfide/thiolate electrolyte and that sulfur was not adsorbed onto the carbon surfaces. The stability of the unannealed carbon was poor in both electrolytes since the adhesion of the film to the substrate was not as good as that of annealed carbon.

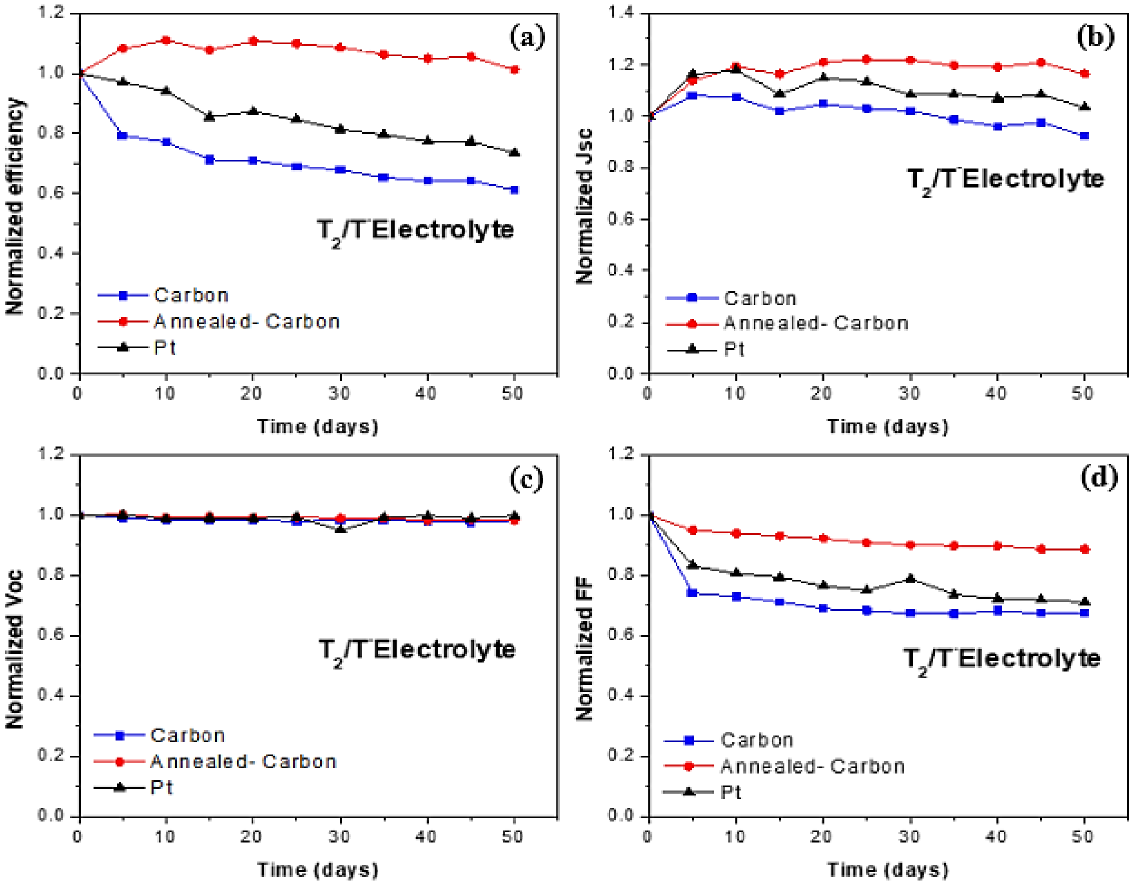

Fig. 10: Normalized (a) efficiency, (b) J_{sc}, (c) V_{oc} and (d) Fill factor of the DSSCs based on T_2/T^- electrolyte.

2.2 Ni3S2@MWCNTs films for effective counter electrodes of dye-sensitized solar cells

Fig. 11 (a) – (c) show the SEM micrographs of all three different CE films obtained by the hydrothermal method. Fig. 11 (a) is a SEM micrograph of a MWCNTs film-coated FTO glass substrate with an expanded view shown in the inset, revealing MWCNTs of approximately 50 nm in diameter coated on the FTO surface. SEM micrograph of a Ni_3S_2 film-coated FTO glass substrate is shown in Fig. 11 (b) with the estimated particle size in the range of 20 - 50 nm, as shown in the inset. It can be seen in Fig. 11 (b) that some of Ni_3S_2 nanoparticles are agglomerated to form clusters with sizes ranging from 100 to 800 nm. A morphology of co-catalyst Ni_3S_2@MWCNTs film-coated FTO glass substrate is presented by the SEM micrograph in Fig. 11 (c). It is clearly seen in the inset of Fig. 11 (c) that Ni_3S_2 nanoparticles congregate on the MWCNTs surface and spread onto the whole FTO surface. From these SEM micrographs, it is suggested that the active surface of co-catalyst Ni_3S_2@MWCNTs CE is improved in comparison with those of pure MWCNTs and pure Ni_3S_2 CEs.

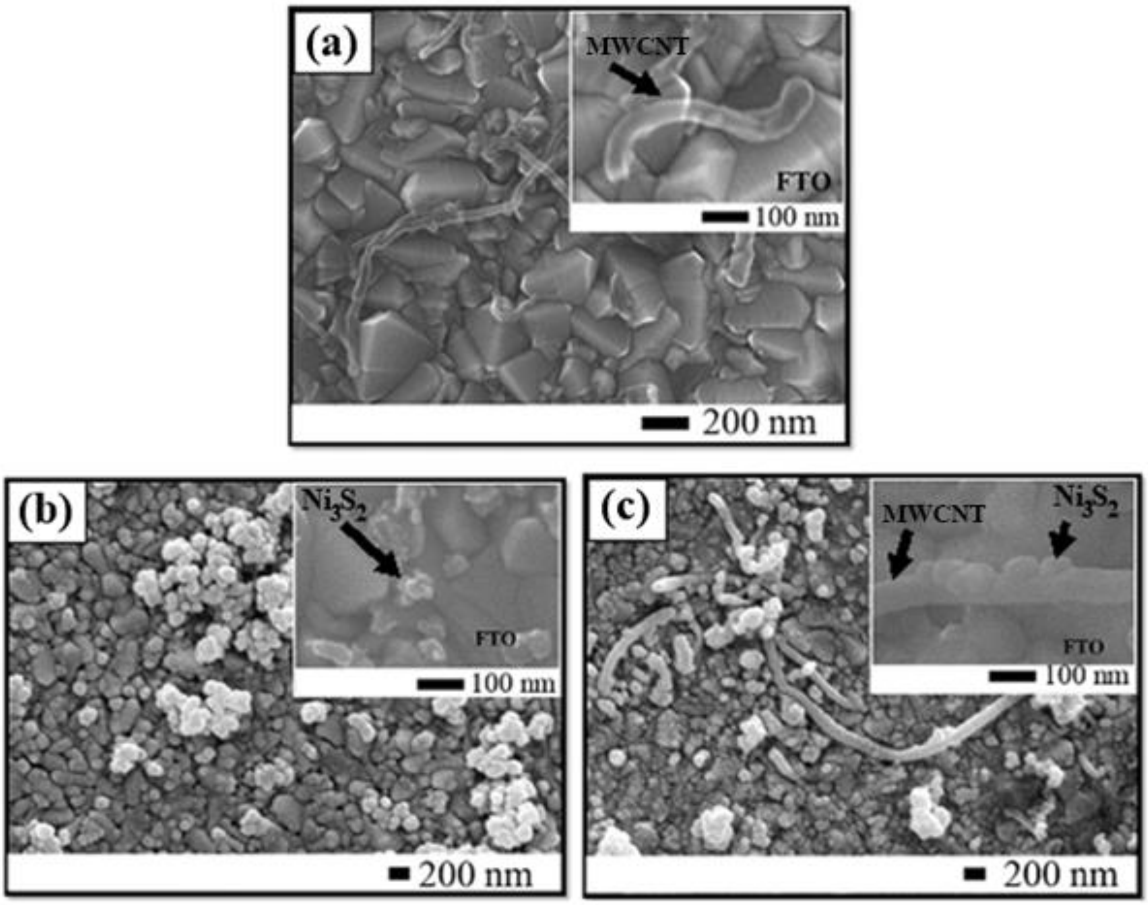

Fig. 11: SEM micrographs of **(a)** MWCNTs, (b) Ni_3S_2 nanoparticles and (c) co-catalyst Ni_3S_2@MWCNTs coated on FTO glass substrate.

The thermogravimetric analysis (TGA) was employed to characterize the thermal stability of Ni_3S_2@MWCNTs composites and determine the weight ratio of MWCNTs and Ni_3S_2. Fig. S1 (in Supporting Information) shows the TGA result of the Ni_3S_2@MWCNTs powder performed in air from 40 ^{O}C to 900 ^{O}C using a heating rate of 10 ^{O}C/min. The weight loss of Ni_3S_2@MWCNTs catalyst appeared from about 80 to 130 ^{O}C due to the evaporation of water. After 150 ^{O}C the decreasing of weight was due to the losses of some functional groups and precursor residues, followed by rapid weight loss due to the burning of MWCNTs. Consequently, the weight ratio of the MWCNTs and Ni_3S_2 was determined and found to be 43/57 %.

The Ni_3S_2 might be attracted on the surface of MWCTs with chemical bonding of C-S. According to their XPS results, Rui Zhang et al. reported that the formation of S-C and C-S bonds might come from the linking between nickel sulfide NPs and the carbon matrix.[15] In our present work, bonding of MWCNT and Ni_3S_2 was analyzed by using FTIR of which the results were shown in Supporting Information Fig. S2. From FTIR spectra of Ni_3S_2@MWCNTs, the transmittance peaks at ~3637, 2115, 1737, 1625, 1369, 1062, 690 and 602-611 cm^{-1} are observed. The peak at 3637 cm^{-1} is characteristic of O-H stretching vibration.[16] The vibration at 2115 cm^{-1} is attributed to a C≡C (alkyne).[17,18] The peak located at 1737 cm^{-1} is assignable to C=O stretching vibration of COOH groups.[19] The peaks located at 1625 cm-1 is indexed to O-H bending mode of the adsorbed water.[20] The peak at1369 cm^{-1} corresponds to CH_3 bond bending of the alkane group.[21] The weak peak at 690 cm^{-1} is suggested to originate from C-S bond.[22] The broad peak at 602-611 cm^{-1} can be assigned to the bending vibration of metal and sulfur (Ni-S bond).[23]

Fig. 12 shows the XRD patterns of all prepared materials. The XRD peaks of MWCNTs located at 26.20^{O}, 42.94^{O}, 44.58^{O} 54.34 and 77.50^{O} correspond to the (002), (100), (101), (004) and (110) crystal planes of the hexagonal graphite phase (ICCD # 00-001-0646), respectively. The XRD peaks of Ni_3S_2 located at 30.82^{O}, 31.11^{O}, 37.56^{O}, 38.40^{O}, 50.08^{O}, 54.61^{O} and 69.01^{O} can be identified to be the (012), (110), (003), (021), (211), (104), and (033) crystal planes of the rhombohedral Ni_3S_2 phase (ICCD # 01-076-1870), respectively. Moreover, the second phase of $NiSO_4 (H_2O)_6$ (ICCD # 01-079-0105) is observed in this sample, which comes from the reactant. In the case of co-catalyst Ni_3S_2@MWCNTs powder, the XRD result shows the dominant diffraction peaks of Ni_3S_2 and MWCNTs.

To compare the electrocatalytic activity of I_3^-/I^- for MWCNTs, Ni_3S_2, Ni_3S_2@MWCNTs and Pt CEs, cyclic voltammetry (CV) was employed for the CE films characterization. The obtained CV curves of these CEs are shown in Fig. 13, revealing the four redox peaks represented by the following reaction,

two oxidation peaks

peak 1, $3I^- - 2e^- = I_3^-$ (3)

peak 2: $2I_3^- - 2e^- = I_2$ (4)

two reduction peaks

peak 3, $3I_2 + 2e^- = I_3^-$ (5)

peak 4, $I_3^- + 2e^- = 3I^-$. (6)

At CE of a DSSC, peak 4 is an important one, because it represents a reaction that a triiodide ion receives electrons from the surface of counter film and becomes an iodide. In addition, the concentration of iodide can affect the short - circuit current (I_{sc}). The relationship between I_{sc} and the iodide concentration [I] is shown in equation (7) [15],

$$I_{sc} = \frac{k_d[I^-]}{k_b[n_0]+k_d[I^-]} q\phi A\Phi \qquad (7)$$

where q is the electric charge, ϕ is the electron injection efficiency, A is the ratio of absorbed photon, Φ is the incident photon flux, k_b is the rate constant for back electron transfer reactions, n_0 is the electron density in TiO_2 and k_d is the rate constant of forward electron transfer reactions. A large iodide concentration can provide a high I_{sc} value and a high DSSC efficiency. In Fig. 13, the Ni_3S_2@MWCNTs CE exhibits a higher absolute current reduction peak than those of the Ni_3S_2 and Pt CEs. Therefore, the Ni_3S_2@MWCNTs CE manifests a good reduction reaction in I_3^-/I^- redox couple electrolyte. Furthermore, the difference between the potential value of the oxidation peak and the reduction peak (ΔE_P) of Ni_3S_2@MWCNTs is 0.20 V, whereas those of Pt and Ni_3S_2 are 0.32 V and 0.37 V, respectively. Since ΔE_P is inversely correlated with the electron transfer rate constant (k_S) i.e., a smaller ΔE_P indicates a higher k_S [16-18]. It is suggested that the superior electrocatalytic activity of Ni_3S_2@MWCNTs is beneficial for solar cell efficiency. Moreover, the good CV of Ni_3S_2@MWCNTs electrode is suggested to originate from its high active surface area and co-catalyst materials of Ni_3S_2 and MWCNTs.

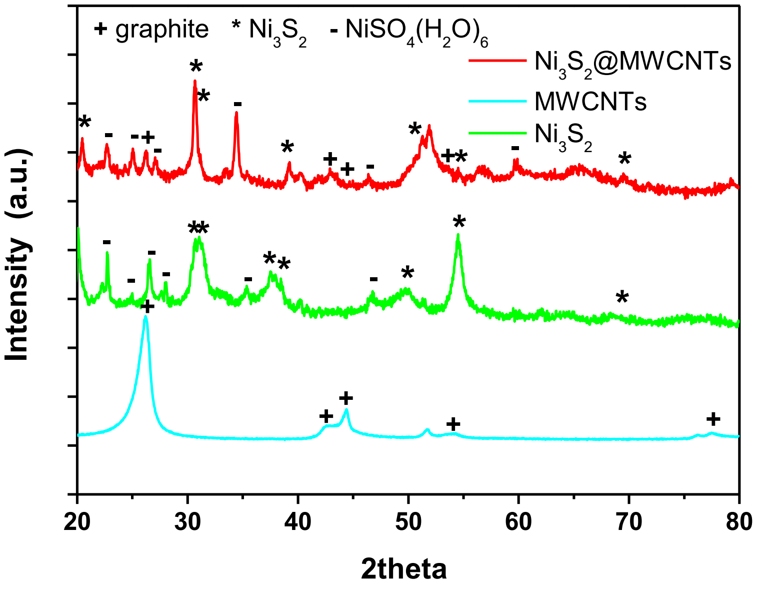

Fig. 12: XRD patterns of MWCNTs, Ni_3S_2 nanoparticles and co-catalyst Ni_3S_2@MWCNTs powder.

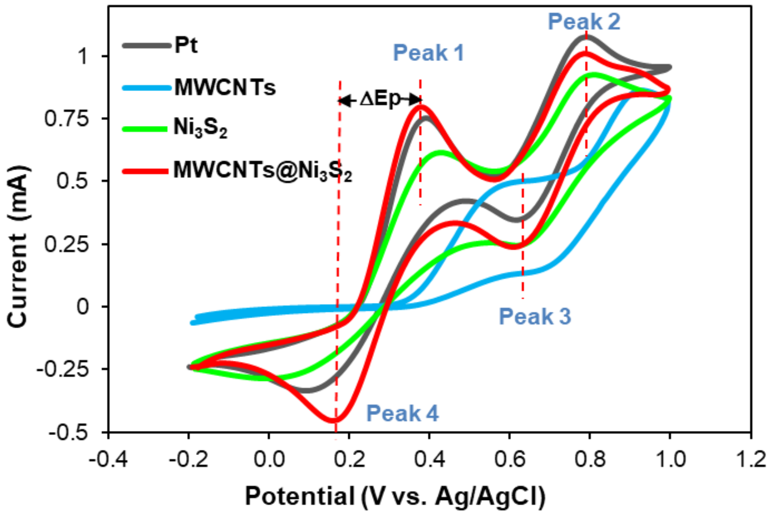

Fig. 13: Cyclic voltammogram (CV) curves of MWCNTs, Ni_3S_2, Ni_3S_2@MWCNTs and Pt CEs at a scan rate of 20 mV/s in a mixture solution of 10 mM LiI, 1 mM I_2, and 0.1 M $LiClO_4$ in acetonitrile.

The active area of each CE was evaluated by the CV technique at different scan rates, based on $K_3Fe(CN)_6$ and KCl electrolytes. The CV curves of Ni_3S_2 and co-catalyst Ni_3S_2@MWCNTs CEs are illustrated in Fig. 14 (a) and (b), respectively. It can be seen that the current of oxidation and reduction peaks increases with the increase of scan rate. These redox currents of $[Fe(CN)_6]^{3-/4-}$ (I_p) vs the square root of the scan rate ($\boldsymbol{U}^{1/2}$) curves of CEs are shown in Fig. 14 (c). In the Randles–Sevcik equation (6), the slope of $\left|I_p\text{-}\boldsymbol{U}^{1/2}\right|$ curve is proportionally related to the active surface area as described in literature [19-20]. According to this equation, the values of *n*, *D* and *C* are kept constant for all samples. The enhancements of I_p-$\boldsymbol{U}^{1/2}$ slopes of the Ni_3S_2@MWCNTs CEs indicate the evolution of the surface area.

$$I_p = 2.65\times10^5 n^{3/2} A D^{1/2} C \boldsymbol{U}^{1/2}, \tag{8}$$

where I_p is the peak current, n is the number of electrons in the reaction, *A* is the electrode area (cm^2), *D* is the diffusion coefficient of the species of interest (cm^2s^{-1}), *C* is the concentration of the species in the bulk solution ($mol^{\cdot}L^{-1}$) and ***U*** is the scan rate (mV/s). Values of the fitted slopes are summarized in Table 4. The absolute reduction and oxidation slopes of the Ni_3S_2@MWCNTs CE are higher than those of pure MWCNTs and Ni_3S_2 CEs. This indicates that the effective surface area of co-catalyst MWCNTs- Ni_3S_2 materials is significantly improved. In general, a large surface area is important for CE, because it can raise the possibility of the triiodide reaction.

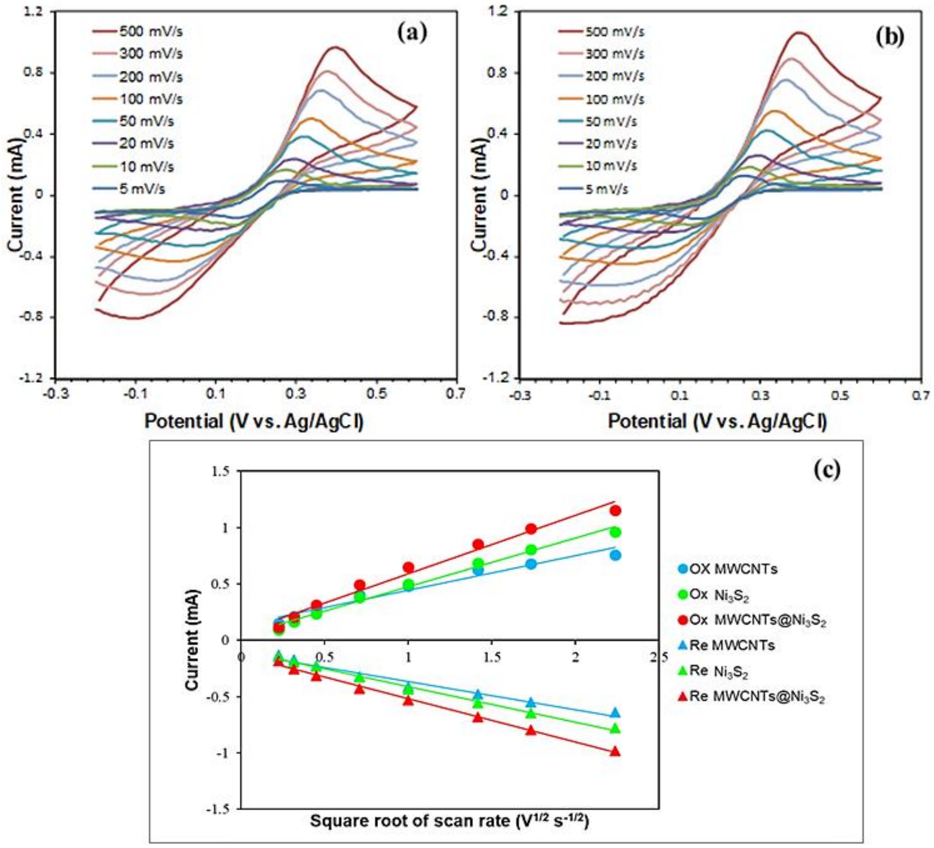

Fig. 14: CV curves of CEs at different scan rates in a mixed solution of 10 mM $K_3(FeCN)_6$ and 0.1 M KCl (a) Ni_3S_2 film, (b) co-catalyst Ni_3S_2@MWCNTs film and (c) plots of the oxidation and reduction currents of $[Fe(CN)_6]^{4-}$ (I_p) vs $\mathbf{U}^{1/2}$ with their corresponding fittings.

Table 4 Summary of series resistance (R_s), charge-transfer resistance at counter electrode/electrolyte (R_{ct}), slope of the oxidation and reduction of I_p-$\mathbf{U}^{1/2}$ curves of MWCNTs, Ni_3S_2 and co-catalyst Ni_3S_2@MWCNTs $_2$ CEs.

Counter	**EIS**					
electrode	**R_S (Ω)**	**R_{ct} (□)**	**R_D (□)**	**C_μ (μF)**	**oxidation**	**reduction**
MWCNTs	15.20	262.62	23.14	0.39	0.31	-0.25
Ni_3S_2	15.61	16.50	5.34	1.68	0.43	-0.31
Ni_3S_2@MWCNTs	16.02	7.25	3.07	2.26	0.52	-0.38
Pt	13.56	22.31	3.13	2.09	-	-

To study the internal charge transfer of these CEs, the EIS was performed to analyze the symmetrical CE (CE-CE) cells under dark condition at the ac current amplitude of 10 mV with a frequency ranging from 0.1 Hz to 100 kHz, and all the EIS spectra of these CEs are presented in Fig. 15 (a). As seen in Fig. 15 (a), each sample reveals two semicircles curve, for which the data are fitted by using Gamry Echem Analyst software in accordance with the equivalent circuit shown in Fig. 15 (b). The equivalent circuit consists of a serie resistance (R_s), an interface charge-transfer resistance (R_{ct}) of the CE/electrolyte, corresponding to the first semicircle in the high frequency region, a constant phase element and a second semicircle in the low frequency region represents the Nernst diffusion impedance (Z_N) of an ion in electrolyte. The obtained EIS values are listed in Table 4. The first parameter R_{ct} relates to the electron transfer during the redox reaction at CE surface between I_3^- and CE. The R_{ct} values can be estimated from the real part of the first semicircle curve. As seen in Fig. 15 (a) and Table 4, the R_{ct} value reduces from 16.50 to 7.25 □ with the MWCNTs loading. Generally, low resistance implies a higher electron transfer rate, leading to the greater power conversion efficiency**.** This means that the co-catalyst Ni_3S_2@MWCNTs CE has a faster electron transport with an excellent electrocatalytic activity for the triiodide electrochemical reaction. Furthermore, the Nernst diffusion resistances (R_D) were calculated from porous bounded Warburg element shown in equation (9).

$$R_D = \frac{B}{Y} \tag{9}$$

Where Y is the magnitude of the admittance at $\omega = 1$ rad/s, and B is the characterized time taken for a reactant to diffuse through a thin film [21]. R_D represent the electron diffusion across the porous of thin film counter electrode in a redox medium. The increasing of diffusion coefficients can be considered from the Nernst diffusion resistances (R_D). Generally, the low R_D represents a high diffusion rate of ions in electrolyte. The Ni_3S_2@MWCNTs counter electrode displayed the lowest R_D, implying the highest diffusion coefficients. At the surface of counter electrode, the triiodide receives electron and becomes iodide ($I_3^- + 2e^- = 3I^-$). The increasing of iodide concentrations from this reduction process could enhance the ion diffusion coefficient in a redox mediate due to This because synergetic effect of co-electrocatalyste materials (Ni_3S_2 and MWCNTs) help improve the electro catalytic activity. Low R_D implies a high tri-iodide/iodide transport. The Ni_3S_2@MWCNTs CE shows a low R_D of 3.07 □. In addition, the double-layer capacitance (C_μ) values are correlated with the effective surface area of counter electrodes. High capacitance implies a large effective surface area as well [22, 23]. Principally, C_μ can be described by a constant phase element of impedance (Z_{CPE}) in equation (10),

$$Z_{CPE} = \frac{1}{(j\omega)^{\alpha} Y_0} \tag{10}$$

Where ω is the angular frequency, Y_0 is the CPE parameter or C_μ, and α is the CPE exponent ($0 \leq \alpha \leq 1$). The C_μ value of Ni_3S_2@MWCNTs, MWCNTs, Ni_3S_2 and Pt CEs were determined and found to be 2.26, 0.39, 1.68 and 2.09 μF, respectively. Consequently, it is suggested that the Ni_3S_2@MWCNTs CE has the largest effective surface area.

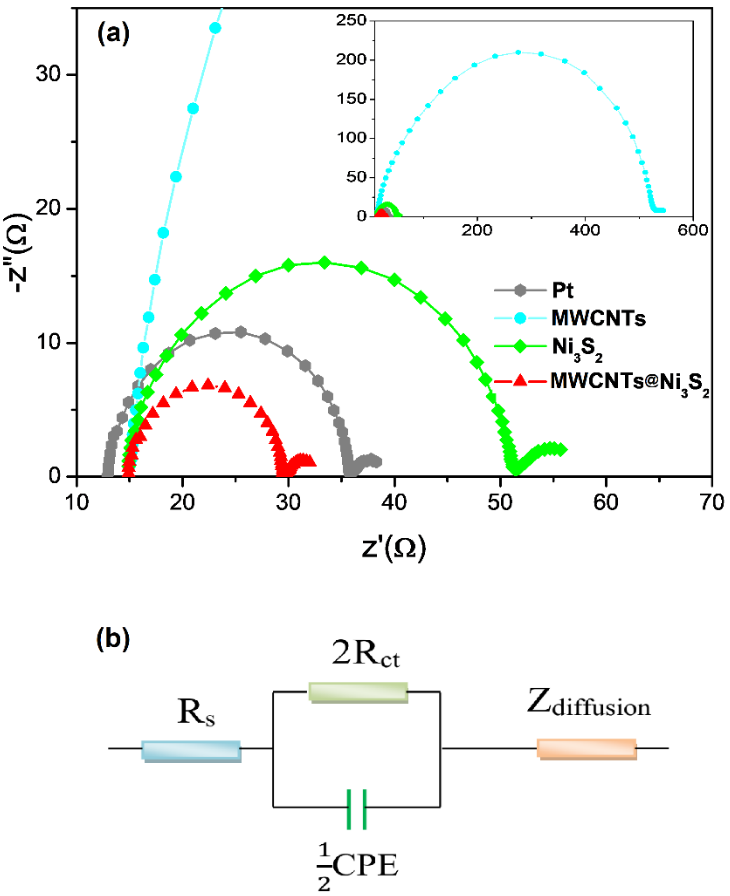

Fig. 15: (a) Nyquist plots of symmetrical cells of Ni_3S_2 and co-catalyst Ni_3S_2@MWCNTs CEs and (b) schematic representation of CE-CE equivalent circuit.

The power conversion efficiency of DSSCs was measured by a solar simulator system (Peccell, PE-L111, Japan) at AM 1.5. Fig. 7 displays the J-V curves of these DSSCs based on CEs made of MWCNTs (MWCNTs-DSSC), Ni_3S_2 (Ni_3S_2-DSSC) and co-catalyst Ni_3S_2@MWCNTs (MWCNTs- Ni_3S_2-DSSC). The energy conversion efficiency (η) and fill factor (FF) of these solar cells were calculated using equation (11) and (12), respectively.

$$\eta = \frac{FF.J_{sc}.V_{oc}}{P_{light}} 100\% \tag{11}$$

$$FF = \frac{J_{max}.V_{max}}{J_{sc}.V_{oc}} \tag{12}$$

Photovoltaic parameters were determined from the J-V curves and the obtained values are summarized in Table 2. From these data, it can be seen that the NiS-DSSC yields a short circuit current density (J_{sc}) of 13.61 mA/cm^2 and the open-circuit voltage (V_{oc}) of 0.74 V, which are less than the J_{sc} (17.25 mA/cm^2) and V_{oc} (0.75 V) of Ni_3S_2@MWCNTs -DSSC. The increase of J_{sc} results in the enhancement of a solar cell performance based on Ni_3S_2@MWCNTs CE (7.48%), which is higher than those of the Ni_3S_2-DSSC (6.21%)

and Pt-DSSC (7.24%). The enhancement of cell efficiency in Ni_3S_2@MWCNTs -DSSC mainly arises from the raise in active surface area of CE, supporting the electrochemical activity of electrode, as confirmed by the increase of the CV slope (shown in Fig. 3 (c)) and co-catalyst Ni_3S_2@MWCNTs materials. As seen in Table 2, MWCNTs-DSSC yields the lowest value of FF (0.24), J_{sc} (11.14 mA/cm^2) and performance (1.66%), which is probably due to the small amount of MWCNTs loading. Moreover, the poor FF of MWCNTs-DSSC indicates a large internal resistance of DSSC.

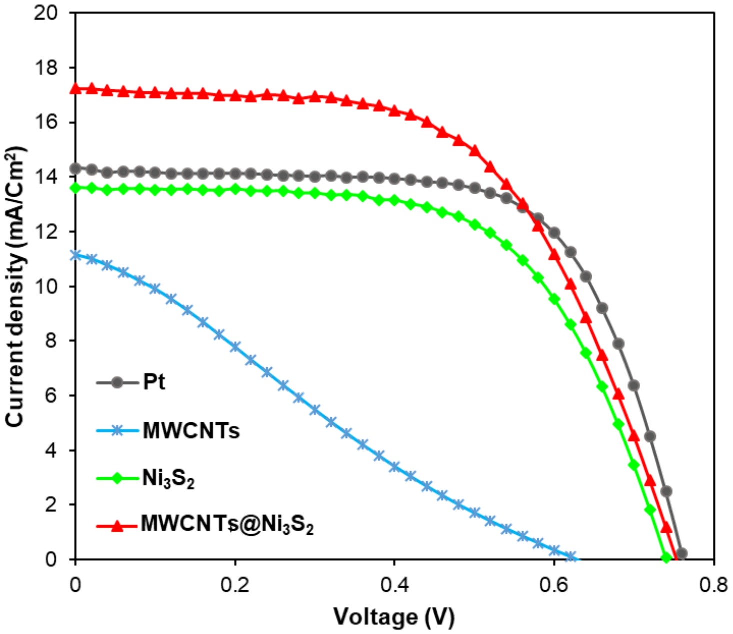

Fig. 16: Plots of photocurrent density **(**J**)** as a function of voltage **(**V**)** for DSSCs based on MWCNTs, Ni_3S_2, co- catalyst Ni_3S_2@MWCNTs and Pt CEs**.**

Table 5 Photovoltaic characteristics of DSSCs based on MWCNTs, Ni_3S_2, co-catalyst Ni_3S_2@MWCNTs and Pt CEs; open circuit voltage (V_{oc}), short circuit current density (J_{sc}), Fill factor (FF) and solar cell efficiency (η).

Counter electrode	**J-V**			
	J_{sc} (mA/cm^2)	**V_{oc} (V)**	**FF**	**η (%)**
Pt	14.33	0.76	0.65	7.24
MWCNTs	11.14	0.63	0.24	1.66
Ni_3S_2	13.61	0.74	0.61	6.21
Ni_3S_2@MWCNTs	17.25	0.75	0.56	7.48

2.3 References

[1] F.C. Tai, S.C. Lee, C.H. Wei, S.L. Tyan, Correlation between ID□IG Ratio from Visible Raman Spectra and sp2/sp3 Ratio from XPS Spectra of Annealed Hydrogenated DLC Film, Mater. Trans. 47 (2006) 1847–1852. doi:10.2320/matertrans.47.1847.

[2] A.C. Ferrari, J. Robertson, Interpretation of Raman spectra of disordered and amorphous carbon, Phys. Rev. B. 61 (2000) 14095–14107. http://link.aps.org/doi/10.1103/PhysRevB.61.14095.

[3] M.A. Tamor, W.C. Vassell, Raman ““fingerprinting”” of amorphous carbon films, J. Appl. Phys. 76 (1994) 3823. doi:10.1063/1.357385.

[4] S. Prawer, K.W. Nugent, D.N. Jamieson, J.O. Orwa, L.A. Bursill, J.L. Peng, The Raman spectrum of nanocrystalline diamond, Chem. Phys. Lett. 332 (2000) 93–97. doi:https://doi.org/10.1016/S0009-2614(00)01236-7.

[5] A.J. Neves, M.H. Nazaré, I. (Information service), I.E. Group, I. of E. Engineers, Properties, Growth and Applications of Diamond, Institution of Electrical Engineers, 2001. https://books.google.co.th/books?id=jtC1mUFZfQcC.

[6] V. Paillard, On the origin of the 1100 cm□1Raman band in amorphous and nanocrystallinesp3carbon, Europhys. Lett. 54 (2001) 194–198. doi:10.1209/epl/i2001-00105-4.

[7] N. Khamnualthong, K. Siangchaew, P. Limsuwan, Thermal Stability Evaluation of Diamond-like Carbon for Magnetic Recording Head Application using Raman Spectroscopy, Procedia Eng. 32 (2012) 888–894. doi:10.1016/j.proeng.2012.02.028.

[8] I. Jung, D.A. Dikin, R.D. Piner, R.S. Ruoff, Tunable Electrical Conductivity of Individual Graphene Oxide Sheets Reduced at “Low” Temperatures, Nano Lett. 8 (2008) 4283–4287. doi:10.1021/nl8019938.

[9] Z.J. Li, B.C. Yang, S.R. Zhang, C.M. Zhao, Graphene oxide with improved electrical conductivity for supercapacitor electrodes, Appl. Surf. Sci. 258 (2012) 3726–3731. doi:10.1016/j.apsusc.2011.12.015.

[10] M. Marton, M. Vojs, E. Zdravecká, M. Himmerlich, T. Haensel, S. Krischok, M. Kotlár, P. Michniak, M. Veselý, R. Redhammer, Raman spectroscopy of amorphous carbon prepared by pulsed arc discharge in various gas mixtures, J. Spectrosc. 1 (2013).

[11] W. Maiaugree, S. Lowpa, M. Towannang, P. Rutphonsan, A. Tangtrakarn, S. Pimanpang, P. Maiaugree, N. Ratchapolthavisin, W. Sang-aroon, W. Jarernboon, V. Amornkitbamrung, A dye sensitized solar cell using natural counter electrode and natural dye derived from mangosteen peel waste, Sci. Rep. 5 (2015) 15230.

[12] A. Hilmi, T.A. Shoker, T.H. Ghaddar, Universal Low-Temperature MWCNT-COOH-Based Counter Electrode and a New Thiolate/Disulfide Electrolyte System for Dye-Sensitized Solar Cells, ACS Appl. Mater. Interfaces. 6 (2014) 8744–8753. doi:10.1021/am501520s.

[13] R.S. Nicholson, Theory and Application of Cyclic Voltammetry for Measurement of Electrode Reaction Kinetics., Anal. Chem. 37 (1965) 1351–1355. doi:10.1021/ac60230a016.

[14] C.-T. Li, C.-T. Lee, S.-R. Li, C.-P. Lee, I.-T. Chiu, R. Vittal, N.-L. Wu, S.-S. Sun, K.-C. Ho, Composite films of carbon black nanoparticles and sulfonated-polythiophene as flexible counter electrodes for dye-sensitized solar cells, J. Power Sources. 302 (2016) 155–163. doi:10.1016/j.jpowsour.2015.10.028.

[15] R. Zhang, C. Lu, Z. Shi, T. Liu, T. Zhai, W. Zhou, Hexagonal phase NiS octahedrons co-modified by 0D-, 1D-, and 2D carbon materials for high-performance supercapacitor, Electrochim. Acta. 311 (2019) 83–91. doi:https://doi.org/10.1016/j.electacta.2019.04.111.

[16] L.-X. Yang, Y.-J. Zhu, H. Tong, Z.-H. Liang, L. Li, L. Zhang, Hydrothermal synthesis of nickel hydroxide nanostructures in mixed solvents of water and alcohol, J. Solid State Chem. 180 (2007) 2095–2101.

[17] M. Abdullah, S.K. Kamarudin, L.K. Shyuan, TiO2 Nanotube-Carbon (TNT-C) as Support for Pt-based Catalyst for High Methanol Oxidation Reaction in Direct Methanol Fuel Cell, Nanoscale Res. Lett. 11 (2016) 553. doi:10.1186/s11671-016-1587-2.

[18] J.K. Kibet, B.C. Mosonik, V.O. Nyamori, S.M. Ngari, Free radicals and ultrafine particulate emissions from the co-pyrolysis of Croton megalocarpus biodiesel and fossil diesel, Chem. Cent. J. 12 (2018) 89.

[19] Y.R. Lee, S.C. Kim, H. Lee, H.M. Jeong, A. V Raghu, K.R. Reddy, B.K. Kim, Graphite oxides as effective fire

retardants of epoxy resin, Macromol. Res. 19 (2011) 66–71. doi:10.1007/s13233-011-0106-7.

[20] S. Bai, K. Zhang, L. Wang, J. Sun, R. Luo, D. Li, A. Chen, Synthesis mechanism and gas-sensing application of nanosheet-assembled tungsten oxide microspheres, J. Mater. Chem. A. 2 (2014) 7927–7934.

[21] A.A. Shamsuri, R. Daik, Utilization of an Ionic Liquid/Urea Mixture as a Physical Coupling Agent for Agarose/Talc Composite Films, Mater. (Basel, Switzerland). 6 (2013) 682–698. doi:10.3390/ma6020682.

[22] C.N.R. Rao, R. Venkataraghavan, T.R. Kasturi, CONTRIBUTION TO THE INFRARED SPECTRA OF ORGANOSULPHUR COMPOUNDS, Can. J. Chem. 42 (1964) 36–42. doi:10.1139/v64-006.

[23] A. Molla, M. Sahu, S. Hussain, Synthesis of Tunable Band Gap Semiconductor Nickel Sulphide Nanoparticles: Rapid and Round the Clock Degradation of Organic Dyes, Sci. Rep. 6 (2016) 26034.

Appendix

Diamond & Related Materials 97 (2019) 107451

Contents lists available at ScienceDirect

Diamond & Related Materials

journal homepage: www.elsevier.com/locate/diamond

High stability arc-evaporated carbon counter electrodes in a dye sensitized solar cell based on inorganic and organic redox mediators

Apishok Tangtrakarn[a,b], Wasan Maiaugree[a,c,*], Pikaned Uppachai[d], Nattawat Ratchapolthavisin[a,b], Klitsada Moolsarn[a], Ekaphan Swatsitang[a,b], Vittaya Amornkitbamrung[a,b]

[a] Department of Physics, Faculty of Science, Khon Kaen University, Khon Kaen 40002, Thailand
[b] Institute of Nanomaterials Research and Innovation for Energy (IN-RIE), NANOTEC -KKU RNN on Nanomaterials Research and Innovation for Energy, Khon Kaen University, Khon Kaen 40002, Thailand
[c] Energy Innovation and Heat Pipe Technology Research Unit, Department of Physics, Faculty of Science, Mahasarakham University, Mahasarakham 44150, Thailand
[d] Department of Applied Physics, Faculty of Engineering, Rajamangala University of Technology Isan, Khon Kaen Campus, Khon Kaen 40000, Thailand

ARTICLE INFO

Keywords:
Dye-sensitized solar cell
Arc evaporation
Carbon films
Counter electrode

ABSTRACT

Carbon films were deposited by an arc evaporation method onto conductive glass and applied as counter electrodes in dye sensitized solar cells (DSSCs). Annealing the carbon films in a N_2 atmosphere contributed to the enhancement of DSSC efficiency because their electrocatalytic activities were significantly enhanced. The efficiency of solar cells with carbon films was 2.37% and 2.75% with an I_3^-/I^- and T_2/T^- electrolyte, respectively. Whilst, that of DSSCs with annealed carbon was increased to 8.04% using I_3^-/I^- and to 4.74% for T_2/T^-. The stability of iodide-based DSSCs was not as high as that of thiolate-based units. Within 50 days, the efficiency of iodide-based DSSC with annealed carbon, Pt and as-deposited carbon dwindled by 20%, 25% and 35%, respectively. After 50 days, the efficiency of DSSCs with annealed carbon employing a disulfide/thiolate electrolyte remained constant, whilst that of DSSCs with as-evaporated carbon and Pt dropped by 26% and 39%, respectively.

1. Introduction

Dye-sensitized solar cells (DSSCs) are most promising renewable energy devices due to their simple manufacturing processes, low toxicity and acceptable performance compare to that of silicon solar cells [1,2]. The three main components of DSSC are its photo-anode (or working electrode), a counter electrode (CE) and an electrolyte [1,3]. Typically, the counter electrodes are platinum (Pt) and Pt/PtO_x [4] due to its good catalytic properties and conductivity that allow high cell efficiency. Unfortunately, Pt is an expensive material and is therefore unsuitable for use in low cost solar cell applications. Therefore, alternative catalytic materials of equivalent properties that are less expensive have been explored to replace Pt CEs. Carbonaceous materials show promise for use as DSSC counter electrodes. Their raw materials are abundant and inexpensive. The use of various forms of carbon have been reported in the literature include graphene [5–9], graphite [10,11], carbon nanotubes [12–14], carbon black [11,15], carbon spheres [14,16] and activated carbon [17]. The most widely used electrolyte for DSSCs is an iodide/triiodide solution. However, this electrolyte has disadvantages in term of corrosiveness, visible-light absorption and sublimation [18]. Cobalt-electrolyte-based DSSCs have been reported by Kakiage et al. These DSSCs achieve efficiencies exceeding 14.3% [19]. Unfortunately, cobalt redox media reveal much lower long-term stability compared to the typical iodide/triiodide electrolyte [20]. An organic disulfide/thiolate was proposed as an alternative electrolyte since it has a negligible corrosion issue. Moreover, it absorbs less visible light [21]. However, when this electrolyte is used with Pt, the efficiency of the resulting DSSC is rather low because it has low fill factor (FF) and a large charge transfer resistance (Rct) [5]. Reducing the Rct by replacing Pt with carbon black and using an electrolyte made of a binary disulfide/thiolate redox couple (T^-/T_2) was attempted. Using carbon black resulted in inhibition of disulfide ion adsorption on the carbon black surface. Therefore, the solar efficiency was successfully increased [22].

In this paper, we used a carbon film from arc evaporation method as a DSSC counter electrode coupled with a disulfide/thiolate electrolyte

---

* Corresponding author at: Integrated Nanotechnology Research Center, Department of Physics, Faculty of Science, Khon Kaen University, Khon Kaen 40002, Thailand.

E-mail address: Wasan.m@msu.ac.th (W. Maiaugree).

https://doi.org/10.1016/j.diamond.2019.107451
Received 13 February 2019; Received in revised form 25 May 2019; Accepted 13 June 2019

that has never before been reported. The phase transformation was studied using Raman spectroscopy and was related to impedance results. It is notable that the phase transformation and solar conversion efficiency of the unannealed films were not reported in any previous study. Additionally, the DSSCs tested with an organic electrolyte disulfide/thiolate (T_2/T^-) were compared to those with an iodide/triiodide electrolyte in terms of their stability.

2. Experimental methods

2.1. Counter electrode preparation

Fluoride-doped tin oxide glass strips (FTO-glass, 7 Ω/sq, Aldrich) were used as substrates for the DSSCs. Carbon films were deposited onto FTO glass using an arc evaporation method, under pressure condition at 26 mTorr and maintained at 30 A for 3 s. A graphite rod (99.96%, Ted Pella) was used as cathode and anode in arc evaporation system. The as-deposited films (carbon films) were subjected to subsequent annealing in nitrogen gas at 500 °C for 5 h to produce annealed-carbon films. The sputtered Pt film was used as a reference counter electrode [23].

2.2. Working electrode preparation

To create a blocking layer, $TiCl_4$ (40 mM in DI water) was deposited on the FTO glass by chemical bath deposition at 70 °C for 30 min. The TiO_2 layers were prepared by coating the FTO glass with TiO_2 pastes PST-18NR and then PST–400C (Catalysts & Chemicals Ind.) on a blocking layer using a screen printing technique. The film was annealed at 500 °C for 1 h. The thickness of the TiO_2 films is about 14 μm and the film is illustrated in Fig. S1. After that, the TiO_2 film was soaked in N719 dye solution (3.5×10^{-4} M in acetonitrile and *tert*-butanol solution at a volume ratio of 1:1) at ambient room temperature for 1 day. The working electrode area was 0.25 cm^2.

2.3. Preparation of electrolyte solution

The inorganic I3-/I- redox mediator contained 0.6 M 1-methyl-3-popylimidazolium iodide (MPI), 0.1 M lithium iodide anhydrous (LiI), 0.05 M iodide (I_2), 0.5 M *tert*-butylpyridine (TBP) and 0.0025 M lithium carbonate ($LiCO_3$) in acetonitrile.

A liquid organic T^-/T_2 redox mediator was prepared by mixing 0.40 M $C_6H_{16}N_5S$ or T^-(5-mercapto-1-methyltetrazole *N*-tetramethylammonium salt) [21], 0.40 M $C_4H_8N_8S_2$ or T_2 (di-5-(1-methyltetrazole)) [21], 0.50 M TBP (4-tert-butylpyridine) and 0.05 M $LiClO_4$ (lithium perchlorate) in an acetonitrile solvent.

2.4. DSSC assembly

The dye-sensitized solar cells were assembled using a closed cell method and an inorganic I_3^-/I^- or organic T^-/T_2 redox mediator was filled into the cells.

2.5. Characterization of the films

The surface structure of carbon and annealed-carbon films were characterized by several techniques. These included field emission scanning electron microscopy (FESEM; JEOL JSM-7001F, Japan). Their morphology and crystallites were studied by transmission electron microscopy (TEM) and selected area electron diffraction (SAED) (TECNAI G^2, the Netherlands), respectively. Raman spectra were obtained using a Raman spectrometry (Horiba JobinYvon T64000, Japan), with a Lexel 95 laser (514.32 nm) as the source for excitation, at a power of 150 mW. The films' chemical and electronic states were examined by X-ray photoelectron spectroscopy (XPS, Kratos Analytical, AXIS ULTRA^{DLD}, UK). The XPS chamber pressure was constant, 2×10^{-9} Torr. The samples were examined in an X-ray hybrid mode using monochromatic Al $K\alpha_{1,2}$ radiation with an energy of 1.4 keV. The spot area was $700 \times 300\ \mu m^2$. The power of the X-ray equipment was maintained at 10 mA and 15 kV. A hemispherical X-ray analyzer was placed at 45° normal to the sample surface. The charging effect was modified using the C 1 s peak (284.6 eV) from an adventitious carbon standard. The catalytic activity of the film with I_3^-/I^- and T^-/T_2 was measured using cyclic voltammetry (CV, Gamry REF 3000, USA) in a three-chamber cell at a 20 mV/s scan rate. A platinum plate and an electrode made from Ag/AgCl were used as the counter and reference electrodes, respectively. A solar simulator was used to determine cell performance (Peccell, PE-L111, Japan) system with a 100 $mW{\cdot}cm^{-2}$ light intensity. Stability tests of DSSC cells were done each day at 25 °C and the average humidity was about 70%. The DSSCs were stored in open box in our laboratory under continuous fluorescent light. The charge transfer resistance of counter electrode impedance was determined using electrochemical impedance spectroscopy (EIS, Gamry REF 3000, USA) where the frequency was varied from 0.05 Hz to 100,000 Hz. The AC amplitude was 10 mV.

3. Results and discussion

The FESEM images showing carbon deposited on FTO glass via an arc evaporation method before and after annealing in N_2 are shown in Fig. 1b and c, respectively. Fig. 1a shows that the pyramidal grains of the fluoride-doped tin oxide film. In Fig. 1b, a thin carbon film shielded the fluoride-doped tin oxide surface. The appearance of carbon morphology before and after annealing were similar.

The structural change of the carbon film subjected to thermal annealing was studied using Raman spectroscopy with 532 cm^{-1} laser excitation. Raman results are given in Fig. 2 and Table 1. It can be clearly seen that the Raman spectrum of the as-deposited film shows a characteristic broad peak that is related to an amorphous structure. The spectra consisted of disordered (D) and graphitic (G) characteristic peaks at around 1350 and 1550 cm^{-1}, respectively. Both peaks are well known as the D-peak (1350 cm^{-1}) and G-peak (1550 cm^{-1}) and are related to disorder carbon and the symmetric E_{2g} mode of graphite-like carbon, respectively [24–26]. The shoulder, located at around 1100 cm^{-1}, is related to Sp^3 bonded carbon atoms having a short range order Sp^3-carbon structure [27–29]. This Sp^3 bond may have been formed during deposition. It could have been transformed into an Sp^2 structure by the annealing process. After annealing in a N_2 atmosphere, the peak intensity of both D (1350 cm^{-1}) and G (1580 cm^{-1}) peaks became stronger. The intensity ratio of the D and G peaks (I_D/I_G) increased from 0.86 to 2.91. Furthermore, the G-peak position, which is related to the Sp^3/Sp^2 ratio, shifted to a higher wavenumber at a higher annealing temperature. This can be attributed to the transformation of an amorphous structure into a crystalline structure by a process called graphitization [25,30].

The atomic bonding structure was determined from XPS. Fig. 3 shows the XPS survey spectra of the as-deposited and annealed carbon films. Both samples contained C1s and O1s. The oxygen content decreased after annealing under a low oxygen atmosphere. The approximate ratio of oxygen to carbon decreased from 0.09 to 0.03. The loss of oxygen could lead to increased film conductivity [31,32]. Fig. 3b and c show high resolution XPS C1s spectra. The Sp^2 and Sp^3 components obtained from the deconvolution of C1s spectra were identified and are summarized in Table 2. The Sp2/Sp3 ratio increased from 2.41 to 3.73 after the film was annealed. The reason for this is due to the increase in a graphite-like phase in the film and the arrangement of Sp2 clusters

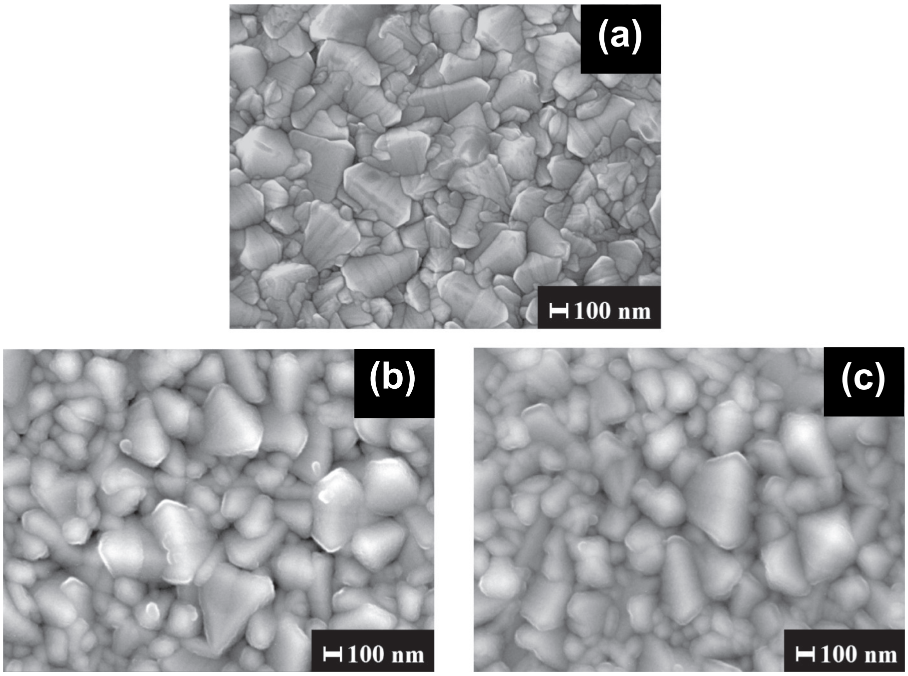

Fig. 1. FESEM images of the (a) FTO-glass, (b) and (c) are those for carbon film and annealed carbon film on FTO glass, respectively.

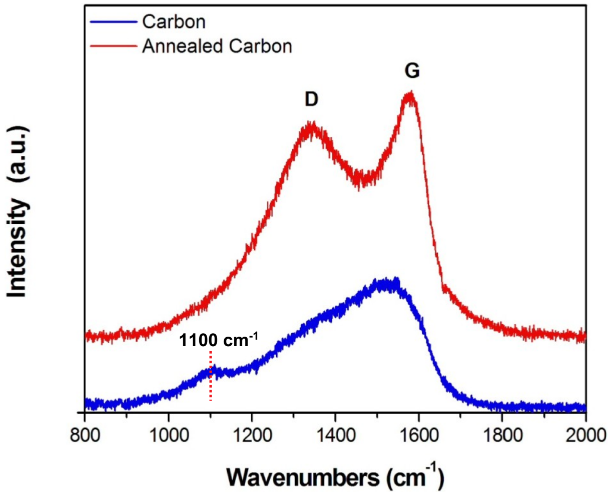

Fig. 2. Raman spectra of the carbon film and annealed carbon film on FTO glass.

Table 1
Information extracted from Raman spectra of carbon films.

Sample	Nanodiamond peak (cm^{-1})	D-peak (cm^{-1})	G-peak (cm^{-1})	FWHM of G-peak	I_D/I_G
Carbon	1100	1350	1534	182.40	0.86
Annealed carbon	–	1350	1580	116.18	2.91

[24,33]. These results agreed well with derived Raman data.

Cyclic voltammetry (CV) was used to analyse the electrochemical reaction of counter electrodes. The CV results of these electrodes in I_3^-/I^- and T_2/T^- are shown in Fig. 4(a) and (b), respectively. For the iodide-based electrolyte, the Pt and annealed carbon counter electrodes presented strong oxidation peak. However, the triiodide reduction peak of annealed-carbon was weaker than that of Pt one. This implies that the electrolytic activity of annealed carbon was lower than that of Pt. The annealed carbon counter electrode exhibited a higher T^- reduction peak than that of Pt in the disulfide/thiolate electrolyte Therefore, annealed carbon exhibited better electrocatalytic activity for reducing disulfide. The reason for this is that Pt was affected by sulfur adsorption on its surface. Pt—S bonds blocked the effective surface area whilst carbon did not behave in this manner [22]. The potential differences between the oxidation and reduction reaction (ΔE_P) was inversely related to the electron transfer rate constant (k_S). A smaller value of ΔE_P corresponded to a higher k_S [34–36]. In the triiodide/iodide system, ΔE_p of Pt was 22 mV, whilst that of annealed carbon was 50 mV. The electron transfer rate of the annealed carbon could have been smaller than that of Pt. Nonetheless, for the disulfide/thiolate system, ΔE_p of annealed carbon (62 mV) was larger than that of Pt (75 mV), implying that the electron transfer rate of annealed carbon was higher than that of Pt. This confirmed that annealing carbon drastically altered the electrochemical characteristics of the as-deposited carbon as the reduction peak was barely evidenced.

Symmetrical counter electrode cells were fabricated for electrochemical impedance spectroscopy (EIS) characterization to analyse the series resistance (R_s), charge transfer resistance (R_{ct}), capacitance (C_μ) and Nernst diffusion (Z_d). The EIS spectra and analysed parameters are shown in Fig. 5 and Table 3, respectively. Simple equivalent circuits, as shown in Fig. 6, were used. Presumably, there are two R_{ct} and one R_{ct} for as-deposited carbon and annealed carbon, respectively. For simplicity, R_{ct} is the total charge transfer resistance ($R_{ct1} + R_{ct2}$) for the carbon sample. From Table 3, the R_s value for annealed carbon was lower than that of the as-deposited carbon for both electrolytes. This was due to the increased content of a graphitic phase. However, the R_s value for both carbon samples was still higher than that of Pt. The EIS spectra for the as-deposited carbon, as shown in Fig. 5, is comprised of two semi-circular arcs. The smaller arc is related to the smaller value of R_{ct}. This parameter should be related to the interfacial resistance between the electrolyte and conductive phase, such as the crystalline graphitic phase that was vaporized from the graphite rod and deposited on the samples. It is notable that there should be a small amount of a

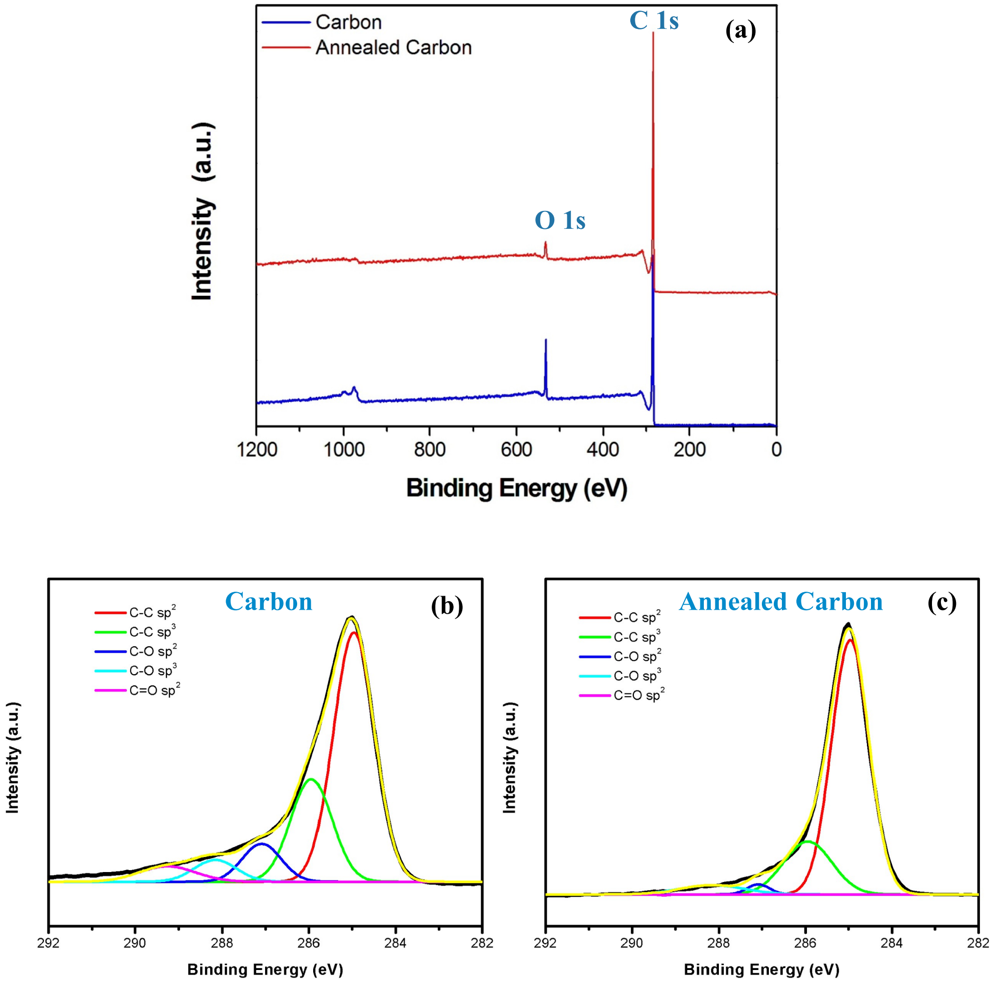

Fig. 3. (a) XPS overview spectra of carbon film and annealed carbon film, (b) and (c) high resolution XPS spectra of the C 1S region of carbon and annealed carbon film, respectively.

graphite phase, since its G-peak was not clear. The other arc, with a larger R_{ct} (R_{ct2}) in the as-deposited carbon, can be attributed to the interfacial resistance between the electrolyte and the less conductive phases, such as amorphous carbon and nanodiamond, whose D and G peaks also appeared in the Raman spectra. For the annealed sample, only one semicircular arc was clearly observed. This is because the amorphous phase and nanodiamond could be transformed to a more graphitic phase. The R_{ct} of annealed carbon (75.5 $\Omega\cdot cm^2$) and as-deposited carbon (493.8 $\Omega\cdot cm^2$) were higher than that of Pt (5.66 $\Omega\cdot cm^2$) using the iodide electrolyte. Nevertheless, for the disulfide/thiolate electrolyte, the R_{ct} of annealed carbon (20.25 $\Omega\cdot cm^2$) was less than that of Pt (38.89 $\Omega\cdot cm^2$) and as-deposited carbon (366.20 $\Omega\cdot cm^2$). This implied that the annealed carbon counter electrodes had a higher electrocatalytic activity than that of a typical Pt counter electrode for the disulfide/thiolate electrolyte, whereas that of Pt was better than that for the anneal carbon in the I_3^-/I^- electrolyte. The trend of impedance results corresponds well with the CV analysis.

The electrocatalytic activity of the counter electrodes can be verified from Tafel polarization of symmetrical cells (Fig. 7). The charge transfer resistance ($R_{ct,\ Tafel}$) is an inverse variable with the exchange current density (J_0) from Tafel polarization following Eq. (1).

$$J_0 = \frac{RT}{nFR_{ct,Tafel}} \tag{1}$$

where R is the gas constant, F is the Faraday constant, T is the absolute temperature and n is the number of electrons participating in the reaction. The trend of $R_{ct,Tafel}$ must follow that of R_{ct} derived from the EIS analysis ($R_{ct,EIS}$) [37]. The $R_{ct,EIS}$ was observed to be the lowest for the iodide-based electrolyte in Pt, resulting in the highest J_0 of Pt. This was confirmed from Tafel polarization. Pt had the highest J_0 value. Moreover, annealed carbon had a higher J_0 value than that of carbon, so the CEs electrocatalytic activity followed the relationship: Pt > annealed carbon > carbon. Using the thiolate-based electrolyte, the highest J_0 was observed for annealed carbon, which was higher than that of Pt.

Table 2
XPS C1s spectra deconvolution of carbon films.

Sample	C–C sp^2 peak (cm^{-1})	C–C sp^3 peak (cm^{-1})	C–O sp^2 peak (cm^{-1})	C–O sp^3 peak (cm^{-1})	C=O sp^2 peak (cm^{-1})	sp^2/sp^3
Carbon	284.96	285.94	287.09	288.15	289.26	2.41
Annealed carbon	284.96	285.94	287.09	288.15	289.26	3.73

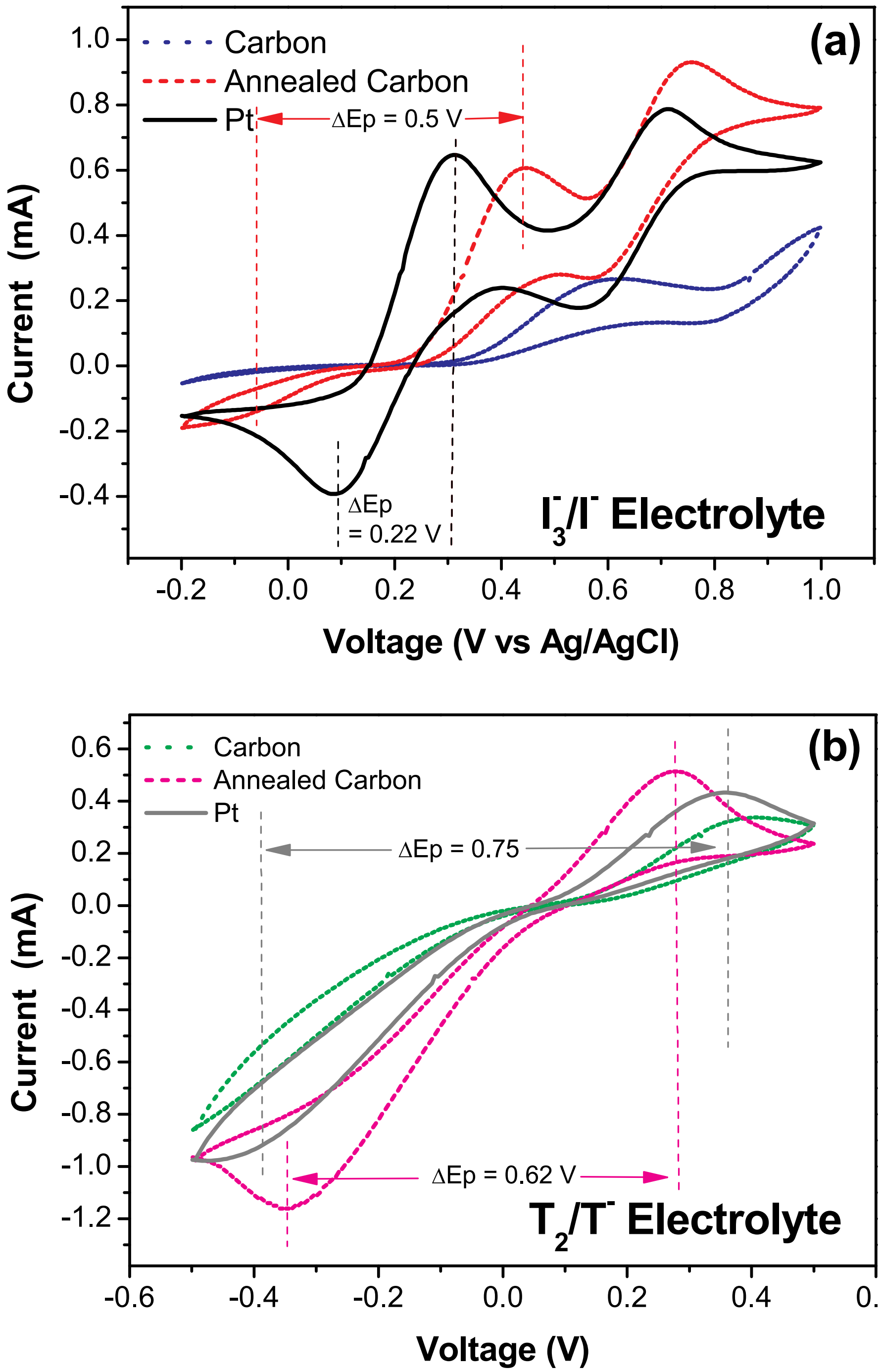

Fig. 4. CV curves of all counter electrodes based on (a) I_3^-/I^- and (b) T_2/T^- electrolytes.

Therefore, the electrocatalytic activity of annealed carbon was higher than that of Pt, in this case.

J-V curves are shown in Fig. 8(a) and (b) for all Pt and carbon DSSCs with triiodide/iodide based and disulfide/thiolate electrolytes, respectively. The related photovoltaic parameters are listed in Table 3. In the case of the iodide electrolyte, the short-circuit current density (J_{sc}) value of the as-deposited carbon, annealed carbon and Pt were 17.72, 18.56 and 18.57 mA/cm^2, respectively. The open-circuit voltage (V_{oc}) value of all samples was around 0.74–0.77 V. Fill factor of annealed carbon (0.64) was close to that of Pt (0.62) and both were higher than that of as-deposited carbon (0.16). The solar efficiency of the DSSC using annealed carbon (8.74%) was close to that of Pt (8.80%) and higher than that of as-deposited carbon (2.11%).

For the T_2/T^- electrolyte, the highest efficiency was achieved for the annealed carbon DSSC (4.74%), compared to those of Pt DSSC (4.18%) and as-deposited carbon DSSC (2.75%). This can be explained by the enhancement of J_{sc} (16.53 mA/cm^2) in the annealed carbon compared to those of Pt (13.51 mA/cm^2) and as-deposited carbon (13.40 mA/cm^2). The V_{oc} for all sample were close to 0.63 V, which was lower than that of the triiodide/iodide system. Moreover, the J_{sc} of anneal carbon in the I_3^-/I^- system was higher than that of the T_2/T^- system. The reduction in V_{oc} and J_{sc} values could result in the reduction of solar efficiency. The FF of annealed carbon (0.45) was close to that of Pt (0.50), but both were higher than that of the as-deposited carbon (0.32). The increase in the J_{sc} and FF values came from the graphitized constituents, resulting in the higher electrocatalytic activity and low

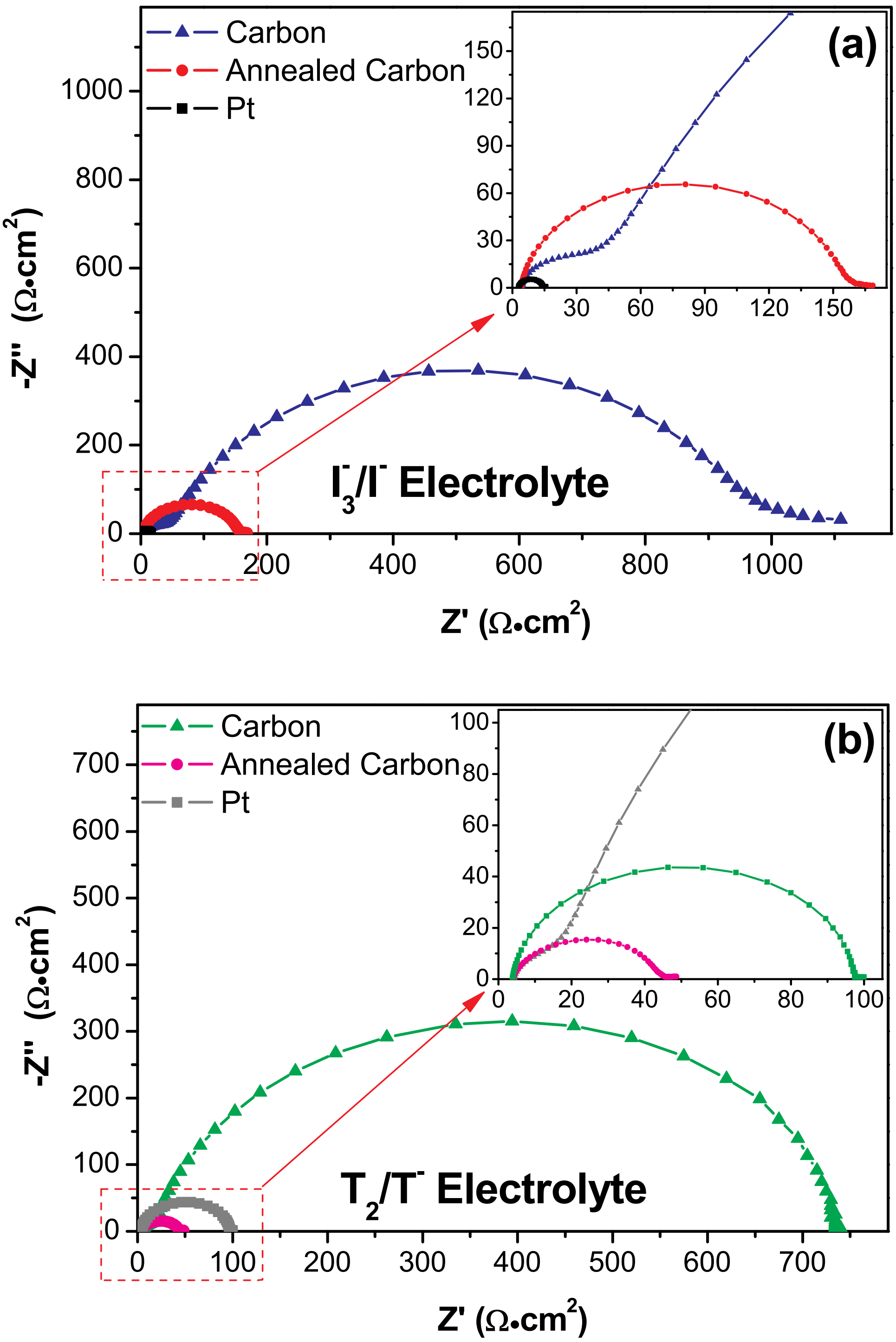

Fig. 5. Nyquist plots for symmetric cells with two identical counter electrodes of the carbon and annealed carbon based on (a) I_3^-/I^- and (b) T_2/T^- electrolytes.

Table 3
Summary of the R_s, R_{ct}, J_{sc}, V_{oc}, FF and η values.

Counter electrode	Electrolyte	EIS				DSSCs				
		R_s (Ω·cm²)	R_{ct1} (Ω·cm²)	R_{ct2} (Ω·cm²)	R_{ct} (R_{ct1} + R_{ct2}) (Ω·cm²)	J_{sc} (mA/cm²)	V_{oc} (V)	FF	η (%)	Average η (%)
Carbon	I_3^-/I^-	4.45	16.30	477.5	493.8	17.72	0.75	0.16	2.11	2.01 ± 0.44
Annealed-carbon	I_3^-/I^-	4.01	75.50	–	75.50	18.56	0.74	0.64	8.74	8.36 ± 0.34
Pt	I_3^-/I^-	3.05	5.66	–	5.66	18.57	0.77	0.62	8.80	8.48 ± 0.30
Carbon	T_2/T^-	4.36	6.20	360.0	366.20	13.40	0.63	0.32	2.75	2.69 ± 0.05
Annealed-carbon	T_2/T^-	3.91	20.25	–	20.25	16.53	0.64	0.45	4.74	4.52 ± 0.23
Pt	T_2/T^-	3.89	46.65	–	38.89	13.51	0.62	0.50	4.18	3.98 ± 0.17

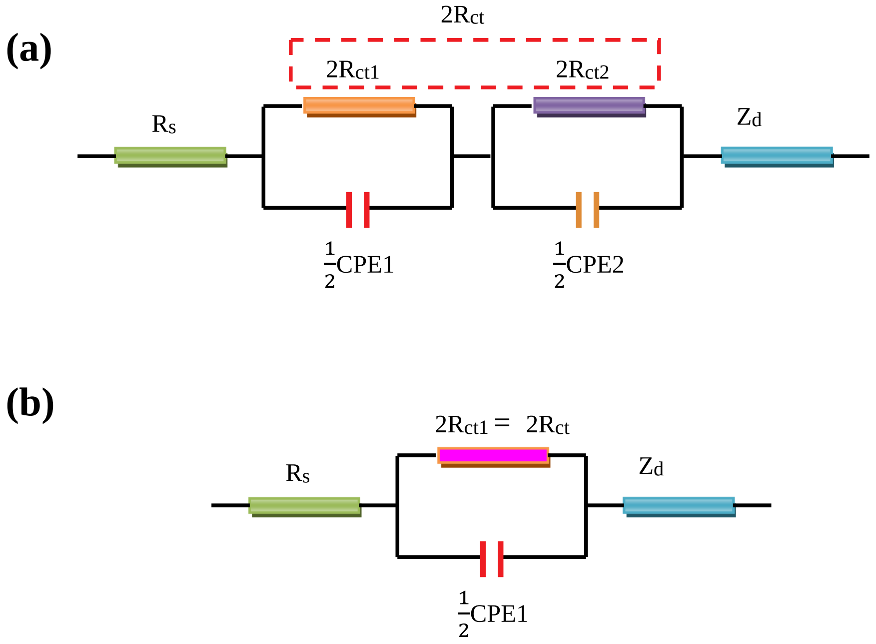

Fig. 6. Equivalent circuit for symmetrical counter electrode of (a) carbon and (b) annealed carbon films.

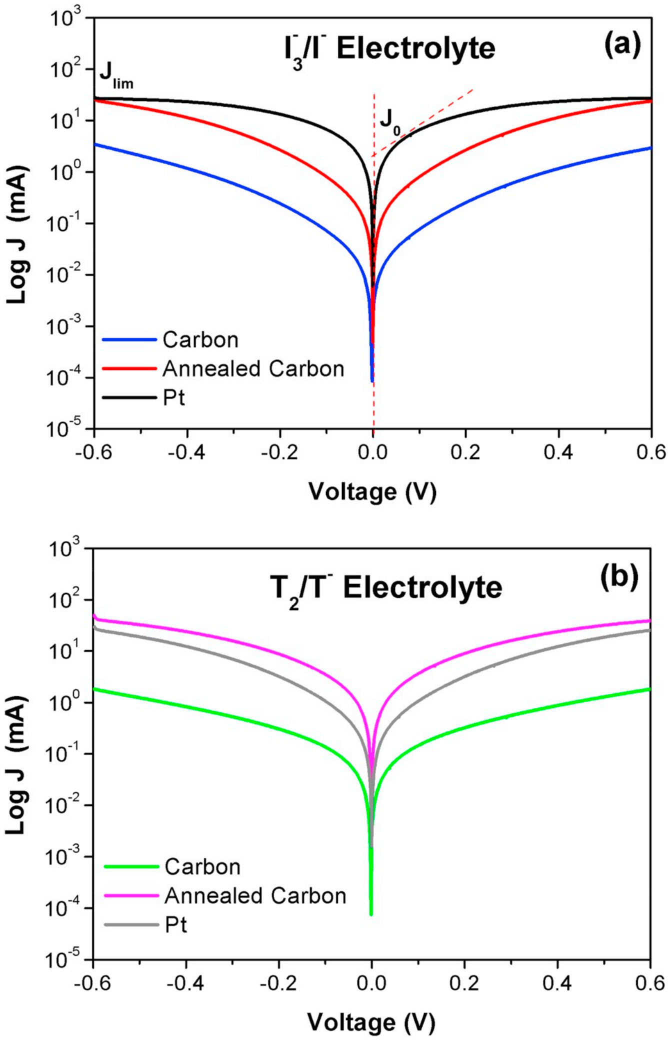

Fig. 7. Tafel curves of the carbon and annealed carbon based on (a) I_3^-/I^- and (b) T_2/T^- electrolytes.

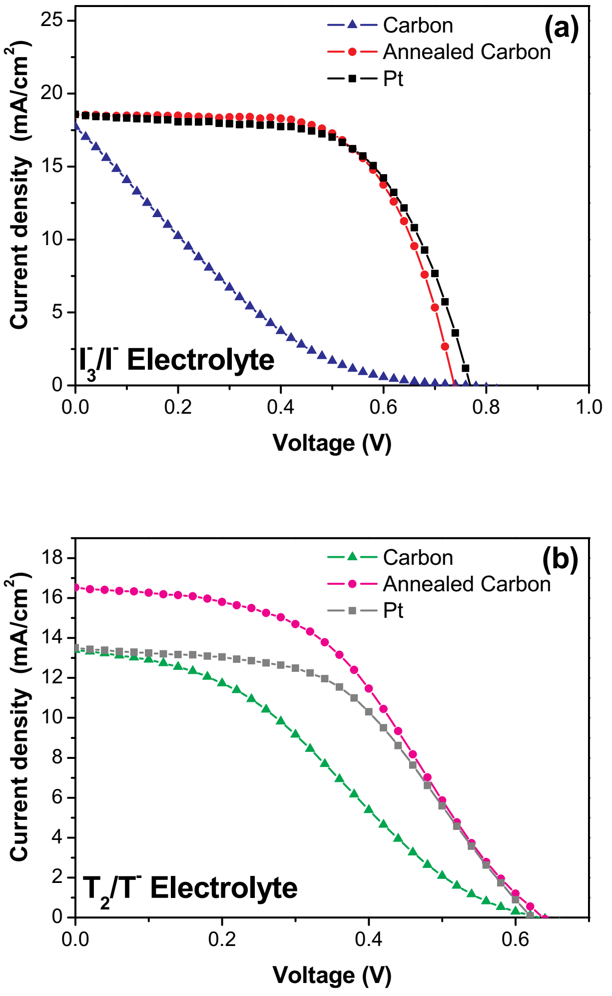

Fig. 8. J–V curves for the DSSCs with the carbon and annealed carbon based on (a) I_3^-/I^- and (b) T_2/T^- electrolytes.

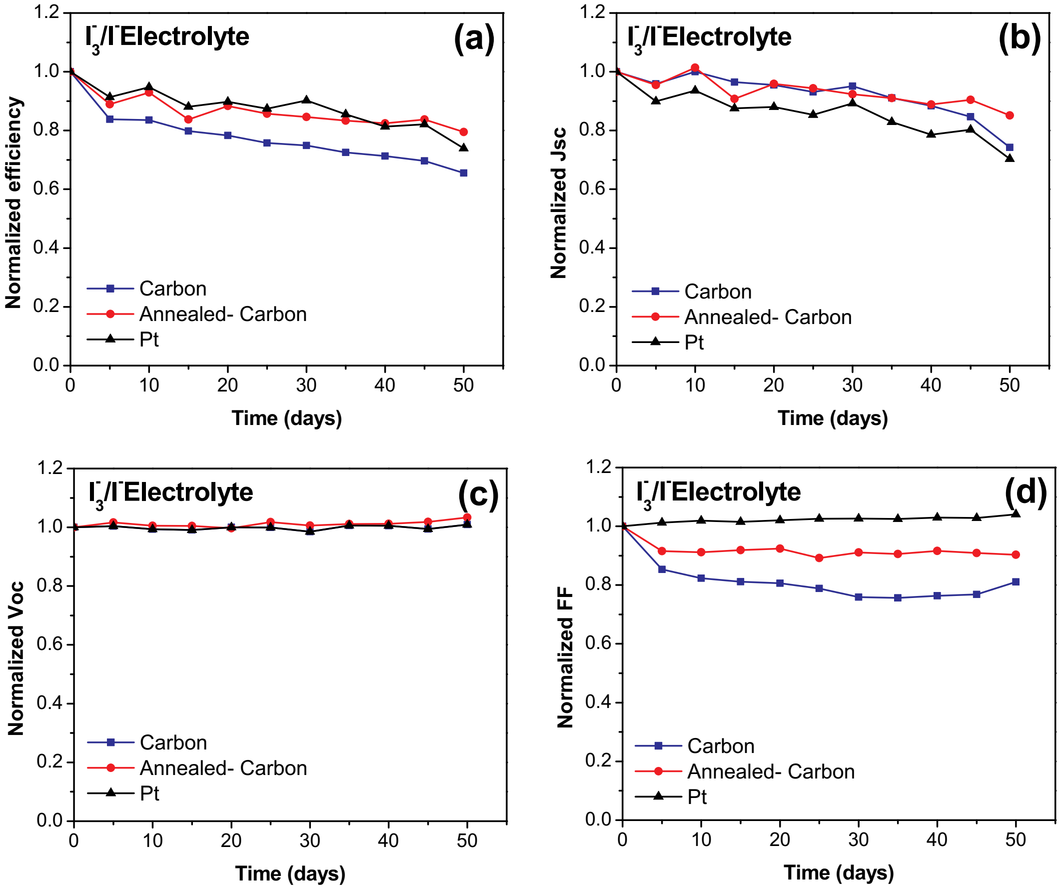

Fig. 9. Normalized (a) efficiency, (b) J_{sc}, (c) V_{oc} and (d) Fill factor of the DSSCs based on I_3^-/I^- electrolyte.

charge transfer resistance. This was confirmed by the CV and EIS results and was similar to that of iodide. These results show the promising potential use of annealed arc-carbon as an alternative counter electrode to replace expensive Pt electrode. Figs. 9 and 10 show the stability tests of DSSC cells. For both electrolytes, the V_{oc} values were quite stable. Comparing FF values of all electrodes in the triiodide electrolyte, it was found that the FF value for Pt infinitesimally changed, whereas those of carbon types were reduced by ~10% for the annealed carbon and ~20% for the as-deposited carbon after the 50th day. However, in the case of the T_2/T^- electrolyte, the reduction of FF values of annealed carbon (~10%) was smaller than those of Pt (~30%) and as-deposited carbon (~30%). In a triiodide/iodide electrolyte, annealed carbon showed a smaller decrease in J_{sc} (10%) than those of other electrodes, ~30% for Pt and ~25% for as-deposited carbon. For the T_2/T^- electrolyte, the J_{sc} values of annealed carbon and Pt changed little, whereas the J_{sc} of as-deposited carbon decreased (10%). The efficiency of all electrodes using an I_3^-/I^- electrolyte had a tendency to decrease with time, resulting in a 20%, 25% and 35% reduction in efficiency for annealed carbon, Pt and as-deposited carbon, respectively. The stability of the annealed carbon film was similar to that of Pt because it is possible for the iodide to be adsorbed on to the surface of carbon, reducing the electrocatalytic activity of the counter electrode, whilst Pt could be vulnerable to iodide corrosion. For the disulfide/thiolate electrolyte, the annealed carbon was stable, so its solar efficiency was infinitesimally affected, whilst Pt and as-deposited carbon showed decreases in solar efficiency of 26% and 39%, respectively. The explanation for this reduction is the formation of Pt—S bonds for disulfide/thiolate electrolyte and that sulfur was not adsorbed onto the carbon surfaces. The stability of the unannealed carbon was poor in both electrolytes since the adhesion of the film to the substrate was not as good as that of annealed carbon.

4. Conclusion

Carbon counter electrodes were prepared using a simple arc evaporation method. A carbon film was annealed in N_2 at 500 °C and compared to the as-deposited film using Raman and XPS techniques. Annealing the film could increase the graphitic phase according to Raman and XPS results as the I_D/I_G and Sp^2/Sp^3 ratios increased. The electrocatalytic activity and the charge-transfer resistance at the counter electrode/electrolyte were determined from CV and EIS results, respectively, in disulfide/thiolate and triiodide/iodide electrolytes. In both electrolytes, the electrocatalytic activity of counter electrode increased and the charge-transfer resistance electrolyte decreased after annealing. These results explained the increase in efficiency of the DSSC using annealed carbon. The efficiency of the annealed carbon DSSC was 8.04% using an I_3^-/I^- electrolyte and 4.74% for the T_2/T^- electrolyte. It is notable that the catalytic activities of T_2/T^- using graphite-like carbon counter electrodes exceeded those using Pt. The stability of DSSCs with annealed carbon was slightly better than that of Pt when the I_3^-/I^- electrolyte was used. However, the annealed carbon counter electrode based on a T_2/T^- electrolyte had a very good stability compared to the Pt counter electrode. In the future, modification of the annealed carbon film may lead to further increase the efficiency of DSSCs.

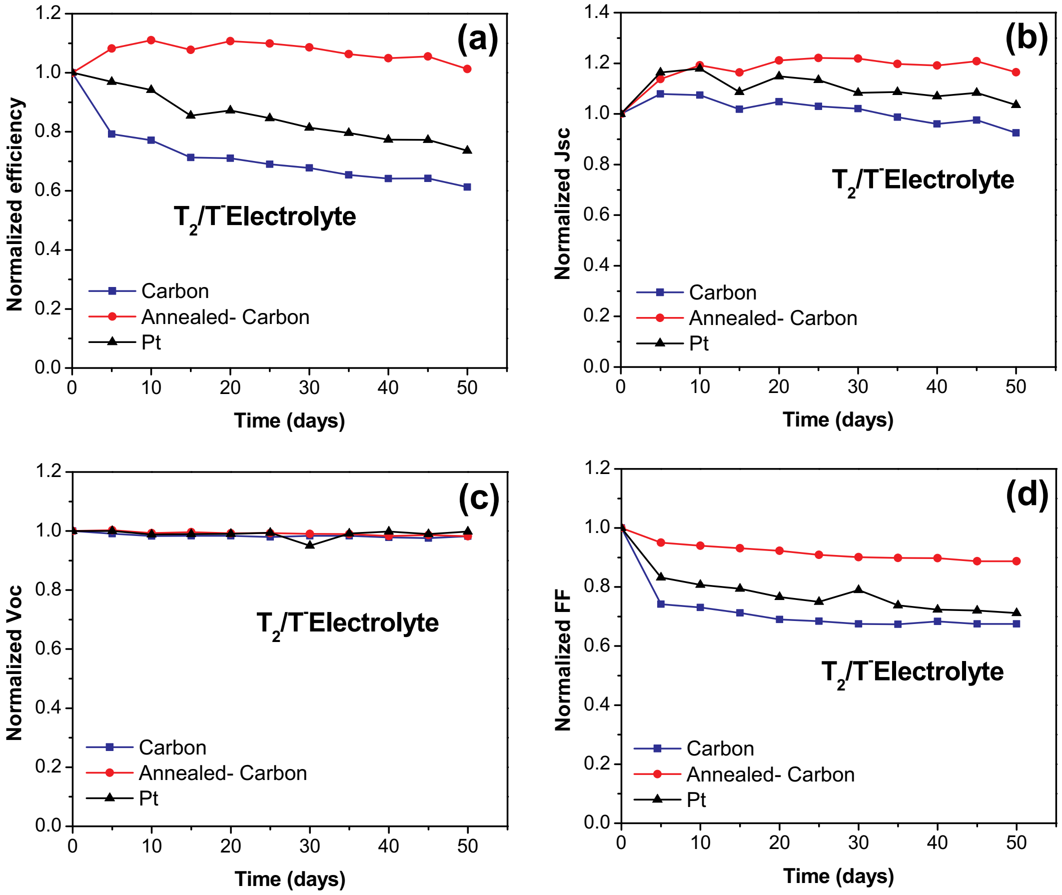

Fig. 10. Normalized (a) efficiency, (b) J_{sc}, (c) V_{oc} and (d) Fill factor of the DSSCs based on T_2/T^- electrolyte.

Acknowledgements

This work was mainly financial supported by the Thailand Research Fund (TRF), The Office of the Higher Education Commission (OHEC) (MRG6180267), Thailand Toray Science Foundation (TTSF). This work also received a scholarship under the Post-doctoral Program from Research Affairs and Graduate School, Khon Kaen University (Grant no. 58227), the Research Network NANOTEC (RNN) program of the National Nanotechnology Center (NANOTEC), NSTDA, Ministry of Science and Technology and Khon Kaen University, Thailand. This research was supported by Mahasarakham University in 2020 and partially supported by Faculty of Science, Mahasarakham University, Thailand.

Appendix A. Supplementary data

Supplementary data to this article can be found online at https://doi.org/10.1016/j.diamond.2019.107451.

References

[1] B. O'Regan, M. Grätzel, A low-cost, high-efficiency solar cell based on dye-sensitized colloidal TiO2 films, Nature 353 (1991) 737–740.

[2] M. Grätzel, The advent of mesoscopic injection solar cells, Prog. Photovolt. Res. Appl. 14 (2006) 429–442, https://doi.org/10.1002/pip.712.

[3] L. Kavan, Electrochemistry and dye-sensitized solar cells, Curr. Opin. Electrochem. 2 (2017) 88–96, https://doi.org/10.1016/j.coelec.2017.03.008.

[4] L. Kavan, H. Krysova, P. Janda, H. Tarabkova, Y. Saygili, M. Freitag, S.M. Zakeeruddin, A. Hagfeldt, M. Grätzel, Novel highly active Pt/graphene catalyst for cathodes of Cu(II/I)-mediated dye-sensitized solar cells, Electrochim. Acta 251 (2017) 167–175, https://doi.org/10.1016/j.electacta.2017.08.080.

[5] J. Burschka, V. Brault, S. Ahmad, L. Breau, M.K. Nazeeruddin, B. Marsan, S.M. Zakeeruddin, M. Gratzel, Influence of the counter electrode on the photovoltaic performance of dye-sensitized solar cells using a disulfide/thiolate redox electrolyte, Energy Environ. Sci. 5 (2012) 6089–6097, https://doi.org/10.1039/C2EE03005E.

[6] W. Yang, X. Xu, L. Hou, X. Ma, F. Yang, Y. Wang, Y. Li, Insight into the topological defects and dopants in metal-free holey graphene for triiodide reduction in dye-sensitized solar cells, J. Mater. Chem. A 5 (2017) 5952–5960, https://doi.org/10.1039/C7TA00278E.

[7] L. Kavan, P. Liska, S.M. Zakeeruddin, M. Grätzel, Low-temperature fabrication of highly-efficient, optically-transparent (FTO-free) graphene cathode for co-mediated dye-sensitized solar cells with acetonitrile-free electrolyte solution, Electrochim. Acta 195 (2016) 34–42, https://doi.org/10.1016/j.electacta.2016.02.097.

[8] L. Kavan, J.-H. Yum, M. Graetzel, Graphene-based cathodes for liquid-junction dye sensitized solar cells: electrocatalytic and mass transport effects, Electrochim. Acta 128 (2014) 349–359, https://doi.org/10.1016/j.electacta.2013.08.112.

[9] L. Kavan, M. Marcaccio, F. Paolucci (Eds.), Exploiting Nanocarbons in Dye-Sensitized Solar Cells BT - Making and Exploiting Fullerenes, Graphene, and Carbon Nanotubes, Springer Berlin Heidelberg, Berlin, Heidelberg, 2014, pp. 53–93, , https://doi.org/10.1007/128_2013_447.

[10] G. Veerappan, K. Bojan, S.-W. Rhee, Sub-micrometer-sized graphite as a conducting and catalytic counter electrode for dye-sensitized solar cells, ACS Appl. Mater. Interfaces 3 (2011) 857–862, https://doi.org/10.1021/am101204f.

[11] P. Yang, Z.-J. Hu, H. Lin, X.-C. Lai, X.-C. Zhao, L.-J. Yang, Ultrasonic remove of particle aggregation in carbon based counter electrodes for dye-sensitized solar cells, J. Nanosci. Nanotechnol. 18 (2018) 4366–4370, https://doi.org/10.1166/jnn.2018.15238.

[12] W.J. Lee, E. Ramasamy, D.Y. Lee, J.S. Song, Performance variation of carbon counter electrode based dye-sensitized solar cell, Sol. Energy Mater. Sol. Cells 92 (2008) 814–818.

[13] J.W. Chew, M.H. Khanmirzaei, A. Numan, F.S. Omar, K. Ramesh, S. Ramesh, Performance studies of ZnO and multi walled carbon nanotubes-based counter electrodes with gel polymer electrolyte for dye-sensitized solar cell, Mater. Sci. Semicond. Process. 83 (2018) 144–149, https://doi.org/10.1016/j.mssp.2018.04.036.

[14] M. Janani, P. Srikrishnarka, S.V. Nair, A.S. Nair, An in-depth review on the role of carbon nanostructures in dye-sensitized solar cells, J. Mater. Chem. A 3 (2015) 17914–17938, https://doi.org/10.1039/C5TA03644E.

[15] P. Li, J. Wu, J. Lin, M. Huang, Y. Huang, Q. Li, High-performance and low platinum loading Pt/carbon black counter electrode for dye-sensitized solar cells, Sol. Energy 83 (2009) 845–849, https://doi.org/10.1016/j.solener.2008.11.012.

[16] W. Wang, J. Yao, X. Zuo, G. Li, High efficiency nitrogen-doped core-shell carbon spheres as counter electrodes for dye-sensitized solar cells, Mater. Lett. 227 (2018)

172–175, https://doi.org/10.1016/j.matlet.2018.05.066.

[17] K. Imoto, K. Takahashi, T. Yamaguchi, T. Komura, J. Nakamura, K. Murata, High-performance carbon counter electrode for dye-sensitized solar cells, Sol. Energy Mater. Sol. Cells 79 (2003) 459–469, https://doi.org/10.1016/S0927-0248(03)00021-7.

[18] H. Tian, X. Jiang, Z. Yu, L. Kloo, A. Hagfeldt, L. Sun, Efficient organic-dye-sensitized solar cells based on an iodine-free electrolyte, Angew. Chem. Int. Ed. Engl. 49 (2010) 7328–7331, https://doi.org/10.1002/anie.201003740.

[19] K. Kakiage, Y. Aoyama, T. Yano, K. Oya, J. Fujisawa, M. Hanaya, Highly-efficient dye-sensitized solar cells with collaborative sensitization by silyl-anchor and carboxy-anchor dyes, Chem. Commun. 51 (2015) 15894–15897, https://doi.org/10.1039/C5CC06759F.

[20] F. Bella, S. Galliano, C. Gerbaldi, G. Viscardi, Cobalt-based electrolytes for dye-sensitized solar cells: recent advances towards stable devices, Energies 9 (2016), https://doi.org/10.3390/en9050384.

[21] M. Wang, N. Chamberland, L. Breau, J.-E. Moser, R. Humphry-Baker, B. Marsan, S.M. Zakeeruddin, M. Grätzel, An organic redox electrolyte to rival triiodide/iodide in dye-sensitized solar cells, Nat. Chem. 2 (2010) 385–389, https://doi.org/10.1038/nchem.610.

[22] W. Cho, D. Song, Y.-G. Lee, H. Chae, Y.R. Kim, Y.B. Pyun, S. Nagarajan, P. Sudhagar, Y.S. Kang, Efficient binary organic thiolate/disulfide redox mediators in dye-sensitized solar cells based on a carbon black counter electrode, J. Mater. Chem. A 1 (2013) 233–236, https://doi.org/10.1039/C2TA00719C.

[23] W. Maiaugree, N. Kongprakaiwoot, A. Tangtrakarn, S. Saekow, S. Pimanpang, V. Amornkitbamrung, Efficiency enhancement for dye-sensitized solar cells with a porous NiO/Pt counter electrode, Appl. Surf. Sci. 289 (2014), https://doi.org/10.1016/j.apsusc.2013.10.100.

[24] F.C. Tai, S.C. Lee, C.H. Wei, S.L. Tyan, Correlation between ID/IG ratio from visible Raman spectra and sp2/sp3 ratio from XPS spectra of annealed hydrogenated DLC film, Mater. Trans. 47 (2006) 1847–1852, https://doi.org/10.2320/matertrans.47.1847.

[25] A.C. Ferrari, J. Robertson, Interpretation of Raman spectra of disordered and amorphous carbon, Phys. Rev. B 61 (2000) 14095–14107 http://link.aps.org/doi/10.1103/PhysRevB.61.14095.

[26] M.A. Tamor, W.C. Vassell, Raman "fingerprinting" of amorphous carbon films, J. Appl. Phys. 76 (1994) 3823, https://doi.org/10.1063/1.357385.

[27] S. Prawer, K.W. Nugent, D.N. Jamieson, J.O. Orwa, L.A. Bursill, J.L. Peng, The Raman spectrum of nanocrystalline diamond, Chem. Phys. Lett. 332 (2000) 93–97, https://doi.org/10.1016/S0009-2614(00)01236-7.

[28] A.J. Neves, M.H. Nazaré, I. (Information service), I.E. Group, I. of E. Engineers, Properties, Growth and Applications of Diamond, Institution of Electrical Engineers, 2001, https://books.google.co.th/books?id=jtC1mUFZfQcC.

[29] V. Paillard, On the origin of the 1100 cm−1Raman band in amorphous and nanocrystallinesp3carbon, Europhys. Lett. 54 (2001) 194–198, https://doi.org/10.1209/epl/i2001-00105-4.

[30] N. Khamnualthong, K. Siangchaew, P. Limsuwan, Thermal stability evaluation of diamond-like carbon for magnetic recording head application using Raman spectroscopy, Procedia Eng. 32 (2012) 888–894, https://doi.org/10.1016/j.proeng.2012.02.028.

[31] I. Jung, D.A. Dikin, R.D. Piner, R.S. Ruoff, Tunable electrical conductivity of individual graphene oxide sheets reduced at "low" temperatures, Nano Lett. 8 (2008) 4283–4287, https://doi.org/10.1021/nl8019938.

[32] Z.J. Li, B.C. Yang, S.R. Zhang, C.M. Zhao, Graphene oxide with improved electrical conductivity for supercapacitor electrodes, Appl. Surf. Sci. 258 (2012) 3726–3731, https://doi.org/10.1016/j.apsusc.2011.12.015.

[33] M. Marton, M. Vojs, E. Zdravecká, M. Himmerlich, T. Haensel, S. Krischok, M. Kotlár, P. Michniak, M. Veselý, R. Redhammer, Raman spectroscopy of amorphous carbon prepared by pulsed arc discharge in various gas mixtures, J. Spectrosc. (2013) 1.

[34] W. Maiaugree, S. Lowpa, M. Towannang, P. Rutphonsan, A. Tangtrakarn, S. Pimanpang, P. Maiaugree, N. Ratchapolthavisin, W. Sang-aroon, W. Jarernboon, V. Amornkitbamrung, A dye sensitized solar cell using natural counter electrode and natural dye derived from mangosteen peel waste, Sci. Rep. 5 (2015) 15230, https://doi.org/10.1038/srep15230.

[35] A. Hilmi, T.A. Shoker, T.H. Ghaddar, Universal low-temperature MWCNT-COOH-based counter electrode and a new thiolate/disulfide electrolyte system for dye-sensitized solar cells, ACS Appl. Mater. Interfaces 6 (2014) 8744–8753, https://doi.org/10.1021/am501520s.

[36] R.S. Nicholson, Theory and application of cyclic voltammetry for measurement of electrode reaction kinetics, Anal. Chem. 37 (1965) 1351–1355, https://doi.org/10.1021/ac60230a016.

[37] C.-T. Li, C.-T. Lee, S.-R. Li, C.-P. Lee, I.-T. Chiu, R. Vittal, N.-L. Wu, S.-S. Sun, K.-C. Ho, Composite films of carbon black nanoparticles and sulfonated-polythiophene as flexible counter electrodes for dye-sensitized solar cells, J. Power Sources 302 (2016) 155–163, https://doi.org/10.1016/j.jpowsour.2015.10.028.

Current Applied Physics 19 (2019) 1355–1361

Contents lists available at ScienceDirect

Current Applied Physics

journal homepage: www.elsevier.com/locate/cap

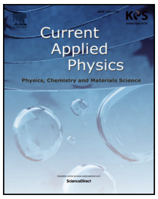

Ni_3S_2@MWCNTs films for effective counter electrodes of dye-sensitized solar cells

Wasan Maiaugree[a,c,*], Tana Tansoonton[a], Vittaya Amornkitbamrung[a,b], Ekaphan Swatsitang[a,**]

[a] Department of Physics, Faculty of Science, Khon Kaen University, Khon Kaen, 40002, Thailand
[b] Institute of Nanomaterials Research and Innovation for Energy (IN-RIE), NANOTEC-KKU RNN on Nanomaterials Research and Innovation for Energy, Khon Kaen University, Khon Kaen, 40002, Thailand
[c] Energy Innovation and Heat Pipe Technology Research Unit, Department of Physics, Faculty of Science, Mahasarakham University, Mahasarakham, 44150, Thailand

ARTICLE INFO

Keywords:
Dye-sensitized solar cell
Ni_3S_2
Multiwall carbon nanotubes
Counter electrode
Hydrothermal method

ABSTRACT

Composite films nickel sulfide (Ni_3S_2) nanoparticles were grown on multiwall carbon nanotubes (MWCNTs) and in situ coated onto conducting glass substrates by the hydrothermal process at 170 °C. These Ni_3S_2@MWCNTs films were applied for counter electrodes (CEs) of dye-sensitized solar cells (DSSCs). In this work, nanostructure, crystalline structure, electrochemical activities and electron-charge transfer resistance of CEs were studied. In addition, the effective surface areas of CEs were analyzed and discussed as well. The power conversion efficiency (PCE) enhancement of up to 7.48%, compared with that of Ni_3S_2-DSSC, was demonstrated for a Ni_3S_2@MWCNTs DSSC.

1. Introduction

Since the first report of dye-sensitized solar cell (DSSC) by O'Regan and Grätzel with the cell efficiency of 8%, intensive study in the past two decades for the improvement of cell performance has become an interesting issue for researchers in the field of photovoltaic cells. Formerly, a highly nanoporous TiO_2, a ruthenium complex and a platinum (Pt) were used as a working electrode (WE), a dye [1] and a counter electrode (CE), respectively. Essentially, most of the effort has been emphasized on the search for other kind of materials to be used as CE and WE, including the replacement of an expensive synthetic dye by natural dyes. In addition, modification of cell structure with the use of different electrolytes has been studied as well. In general, a semiconductor TiO_2 nanoparticles are extensively used as CE of a DSSC due to their practical applicability and provide a cell of the highest energy conversion efficiency. In fact, CE is considered to be an important part of a DSSC due to its key function of transferring electrons to the electrolyte through an iodide/triiodide redox reaction. Generally, the best catalytic agent for CE is an expensive Pt metal. Therefore, the search for new catalytic materials to replace the Pt one is preferable. So far, various alternative catalytic materials such as carbon of different structures and morphologies, metal nitrides, metal sulfides, metal carbides, metal oxides and some kinds of conductive polymers have been applied for CEs of a low-cost DSSC with high performance. Indeed, carbon is the first alternative catalytic material to be used as a CE [2,3] of DSSC and it is everlasting until now [4,5]. Subsequently, conductive polymers such as polyaniline polypyrole and poly (3,4-ethylendioxythiophene) - polystyrene sulfonate (PEDOT-PSS) were employed in the I_3^-/I^- electrolytes for CEs of DSSCs [6–8]. Moreover, carbon of various morphologies and structures such as graphene and carbon nanotubes (CNTs) has been extensively used in DSSC [9–11]. Furthermore, metal-nitrile materials e.g. TiN, Mo_2N and W_2N were used as CEs in high efficiency solar cells by Chen. et al. [12,13]. Additionally, some of metal sulfides e.g. NiS, Ni_3S_2 and CoS had been attempted as electrocatalytic materials for CEs [14–16]. Moreover, other materials that have been attempted for CE are transition metal oxides (ZrO_2 and V_2O_3) [17], metal carbides (WC and SiC) [18,19] and metal selenides ($NiSe_2$ and CoSe) [20,21]. Furthermore, some co-catalytic materials such as CNTs/Pt [22], CNTs/WS_2 [23], CNTs-TiN [24], graphene/Pt [25], graphene/MoS [26] and graphene/FeS_2 [27] have been applied for CEs. For instance, Xiao et al. fabricated nickel sulfide (NiS)/multi-wall carbon nanotubes (MWCNTs) CEs by two steps, i.e. MWCNTs was firstly deposited onto a titanium (Ti) foil substrate using the electrophoresis, after that a pulse potentiostatic technique was used to deposit a nanocrystalline NiS on the MWCNTs [28]. The performance of this NiS/MWCNTs/Ti DSSC could be enhanced to 7.90% as compared with 6.36% of Pt/Ti DSSC.

In this work, we present a novel approach to prepare metal sulfide

---

[*] Corresponding author. Department of Physics, Faculty of Science, Mahasarakham University, Mahasarakham, 44150, Thailand.
[**] Corresponding author. Department of Physics, Faculty of Science, Khon Kaen University, Khon Kaen, 40002, Thailand.
E-mail addresses: wasan.m@msu.ac.th (W. Maiaugree), ekaphan@kku.ac.th (E. Swatsitang).

https://doi.org/10.1016/j.cap.2019.08.020
Received 12 May 2019; Received in revised form 4 August 2019; Accepted 21 August 2019

functionalized multiwall carbon nanotubes CEs. Accordingly, Ni_3S_2@MWCNTs CEs were fabricated by a simple hydrothermal process for the first time. Interestingly, co-catalytic materials can improve electrocatalytic activities i.e. triiodide can receive electron from both MWCNTs and Ni_3S_2. Cyclic voltammogram and electrochemical impedance spectroscopy were employed for the study of cell performance of CE catalytic activity and conductivity, respectively.

2. Experimentals

2.1. Working electrodes

In order to obtain a blocking layer in a DSSC, titanium IV isopropoxide solution (4 mM in isopropanol) was dropped on fluoride doped tin oxide glass substrates (FTO-glass) and spun at1000 rpm for 30 s. After that, they were heated at 80 °C for 5 min. Then, transparent layer of TiO_2 PST-18NR and scattering layer of TiO_2 PST-400C were subsequently coated on these blocking layers by a screen printing method. Next, the TiO_2 films were annealed at 500 °C for 1 h. Finally, these films were soaked in 0.35 mM N719 dye solution at 25 °C for 24 h.

2.2. Counter electrodes

Carboxyl functional groups were generated on multiwall carbon nanotubes (MWCNTs) surfaces by soaking MWCNTs in H_2SO_4 and HNO_3 acids (ratio 3:1 V/V) at room temperature. MWCNTs CEs were fabricated using the mixture of 0.2 g MWCNTs in 30 ml deionized (DI) water for hydrothermal treatment at 170 °C for 24 h. For the preparation of Ni_3S_2 CE, a well-mixed solution of 15 mM sodium hydroxide (NaOH), 12 mM thioacetamide and 10 mM nickel(II) sulfate hexahydrate ($NiSO_4(H_2O)_6$) in DI water was hydrothermally treated at 170 °C for 24 h. Similarly, a co-catalyst Ni_3S_2@MWCNTs CE was prepared by the same process and conditions in the mixture of 0.2 g of MWCNTs with 10 mM $NiSO_4(H_2O)_6$, 15 mM NaOH and 12 mM thioacetamide in 30 ml DI water. All of these obtained films were washed with DI water and dried at 85 °C in an oven. The schematic formation of Ni_3S_2@MWCNTs films are shown in Fig. 1.

2.3. DSSCs assembly

The dye sensitized solar cells were assembled by a semi-closed method using the liquid electrolyte as described in our previous work [42].

3. Results and discussion

Fig. 2 (a) – (c) show the SEM micrographs of all three different CE films obtained by the hydrothermal method. Fig. 2 (a) is a SEM micrograph of a MWCNTs film-coated FTO glass substrate with an expanded view shown in the inset, revealing MWCNTs of approximately 50 nm in diameter coated on the FTO surface. SEM micrograph of a Ni_3S_2 film-coated FTO glass substrate is shown in Fig. 2 (b) with the estimated particle size in the range of 20–50 nm, as shown in the inset. It can be seen in Fig. 2 (b) that some of Ni_3S_2 nanoparticles are agglomerated to form clusters with sizes ranging from 100 to 800 nm. A morphology of co-catalyst Ni_3S_2@MWCNTs film-coated FTO glass substrate is presented by the SEM micrograph in Fig. 2 (c). It is clearly seen in the inset of Fig. 2 (c) that Ni_3S_2 nanoparticles congregate on the MWCNTs surface and spread onto the whole FTO surface. From these SEM micrographs, it is suggested that the active surface of co-catalyst Ni_3S_2@MWCNTs CE is improved in comparison with those of pure MWCNTs and pure Ni_3S_2 CEs.

The thermogravimetric analysis (TGA) was employed to characterize the thermal stability of Ni_3S_2@MWCNTs composites and determine the weight ratio of MWCNTs and Ni_3S_2. Fig. S1 (in Supporting Information) shows the TGA result of the Ni_3S_2@MWCNTs powder performed in air from 40 °C to 900 °C using a heating rate of 10 °C/min. The weight loss of Ni_3S_2@MWCNTs catalyst appeared from about 80 to 130 °C due to the evaporation of water. After 150 °C the decreasing of weight was due to the losses of some functional groups and precursor residues, followed by rapid weight loss due to the burning of MWCNTs. Consequently, the weight ratio of the MWCNTs and Ni_3S_2 was determined and found to be 43/57%.

The Ni_3S_2 might be attracted on the surface of MWCTs with chemical bonding of C–S. According to their XPS results, Rui Zhang et al. reported that the formation of S–C and C–S bonds might come from the linking between nickel sulfide NPs and the carbon matrix [30]. In our present work, bonding of MWCNT and Ni_3S_2 was analyzed by using FTIR of which the results were shown in Supporting Information Fig. S2. From FTIR spectra of Ni_3S_2@MWCNTs, the transmittance peaks at ~3637, 2115, 1737, 1625, 1369, 1062, 690 and 602-611 cm^{-1} are observed. The peak at 3637 cm^{-1} is characteristic of O–H stretching vibration [31]. The vibration at 2115 cm^{-1} is attributed to a $C{\equiv}C$ (alkyne) [32,33]. The peak located at 1737 cm^{-1} is assignable to $C{=}O$ stretching vibration of COOH groups [34]. The peaks located at 1625 cm^{-1} is indexed to O–H bending mode of the adsorbed water [35]. The peak at 1369 cm^{-1} corresponds to CH_3 bond bending of the alkane group [36]. The weak peak at 690 cm^{-1} is suggested to originate from C–S bond [37]. The broad peak at 602-611 cm^{-1} can be assigned to the bending vibration of metal and sulfur (Ni–S bond) [38].

Fig. 3 shows the XRD patterns of all prepared materials. The XRD peaks of MWCNTs located at 26.20°, 42.94°, 44.58° 54.34 and 77.50° correspond to the (002), (100), (101), (004) and (110) crystal planes of the hexagonal graphite phase (ICCD # 00-001-0646), respectively. The

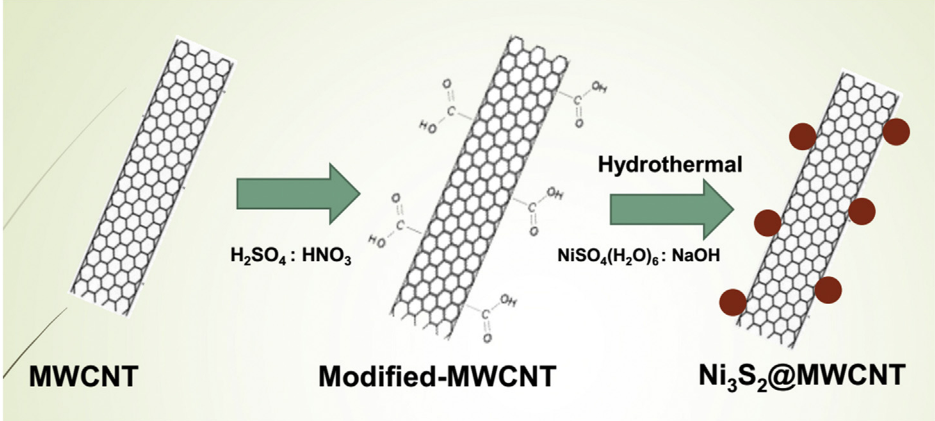

Fig. 1. Schematic illustration to show the formation of Ni_3S_2@MWCNTs films.

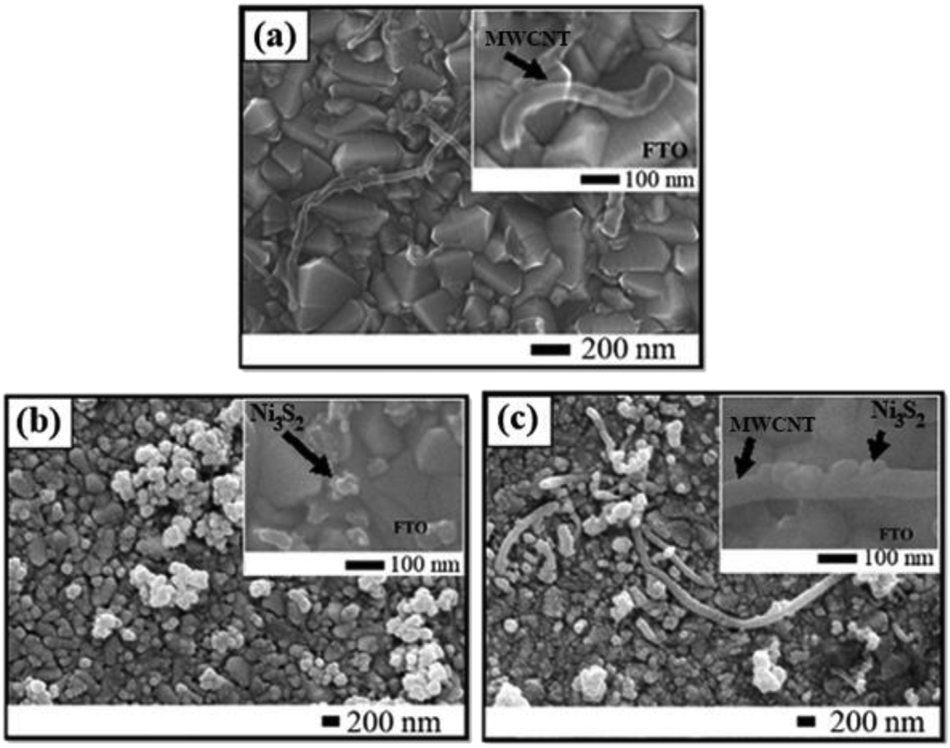

Fig. 2. SEM micrographs of (a) MWCNTs, (b) Ni_3S_2 nanoparticles and (c) co-catalyst Ni_3S_2@MWCNTs coated on FTO glass substrate.

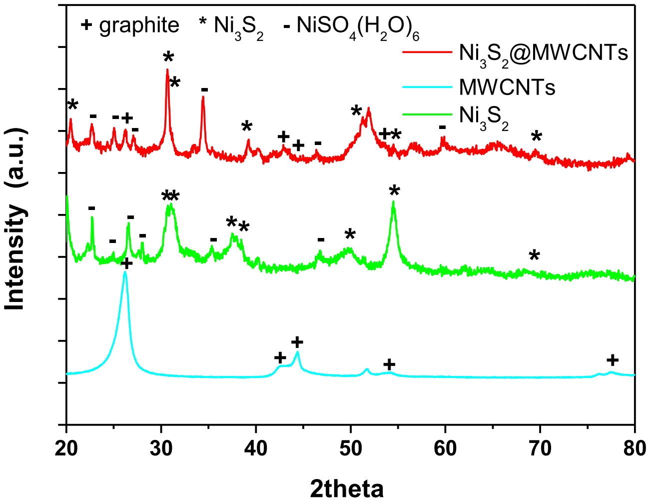

Fig. 3. XRD patterns of MWCNTs, Ni_3S_2 nanoparticles and co-catalyst Ni_3S_2@MWCNTs powder.

XRD peaks of Ni_3S_2 located at 30.82°, 31.11°, 37.56°, 38.40°, 50.08°, 54.61° and 69.01° can be identified to be the (012), (110), (003), (021), (211), (104), and (033) crystal planes of the rhombohedral Ni_3S_2 phase (ICCD # 01-076-1870), respectively. Moreover, the second phase of $NiSO_4$ $(H_2O)_6$ (ICCD # 01-079-0105) is observed in this sample, which comes from the reactant. In the case of co-catalyst Ni_3S_2@MWCNTs powder, the XRD result shows the dominant diffraction peaks of Ni_3S_2 and MWCNTs.

To compare the electrocatalytic activity of I_3^-/I^- for MWCNTs, Ni_3S_2, Ni_3S_2@MWCNTs and Pt CEs, cyclic voltammetry (CV) was employed for the CE films characterization. The obtained CV curves of these CEs are shown in Fig. 4, revealing the four redox peaks represented by the following reaction.

Two oxidation peaks

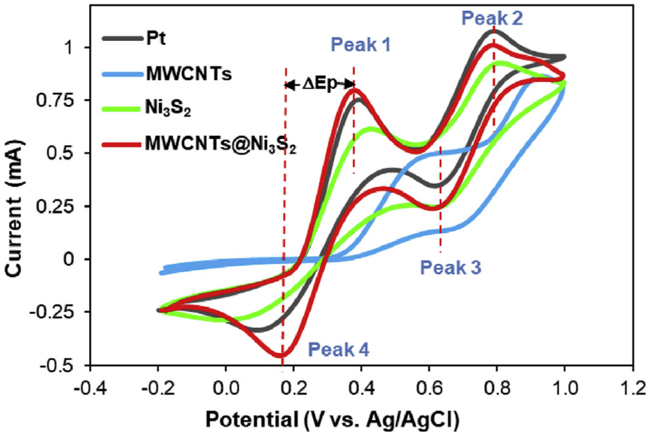

Fig. 4. Cyclic voltammogram (CV) curves of MWCNTs, Ni_3S_2, Ni_3S_2@MWCNTs and Pt CEs at a scan rate of 20 mV/s in a mixture solution of 10 mM LiI, 1 mM I_2, and 0.1 M $LiClO_4$ in acetonitrile.

peak 1, $3I^- - 2e^- = I_3^-$ (1)

peak 2: $2I_3^- - 2e^- = I_2$ (2)

Two reduction peaks

peak 3, $3I_2 + 2e^- = I_3^-$ (3)

peak 4, $I_3^- + 2e^- = 3I^-$. (4)

At CE of a DSSC, peak 4 is an important one, because it represents a reaction that a triiodide ion receives electrons from the surface of counter film and becomes an iodide. In addition, the concentration of iodide can affect the short - circuit current (I_{sc}). The relationship between I_{sc} and the iodide concentration $[I^-]$ is shown in equation (5) [39],

$$I_{sc} = \frac{k_d[I^-]}{k_b[n_0] + k_d[I^-]} q\varphi A\Phi \tag{5}$$

where q is the electric charge, φ is the electron injection efficiency, A is the ratio of absorbed photon, Φ is the incident photon flux, k_b is the rate constant for back electron transfer reactions, n_0 is the electron density in TiO_2 and k_d is the rate constant of forward electron transfer reactions. A large iodide concentration can provide a high I_{sc} value and a high DSSC efficiency. In Fig. 4, the Ni_3S_2@MWCNTs CE exhibits a higher absolute current reduction peak than those of the Ni_3S_2 and Pt CEs. Therefore, the Ni_3S_2@MWCNTs CE manifests a good reduction reaction in I_3^-/I^- redox couple electrolyte. Furthermore, the difference between the potential value of the oxidation peak and the reduction peak (ΔE_P) of Ni_3S_2@MWCNTs is 0.20 V, whereas those of Pt and Ni_3S_2 are 0.32 V and 0.37 V, respectively. Since ΔE_P is inversely correlated with the electron transfer rate constant (k_S) i.e., a smaller ΔE_P indicates a higher k_S [40–42]. It is suggested that the superior electrocatalytic activity of Ni_3S_2@MWCNTs is beneficial for solar cell efficiency. Moreover, the good CV of Ni_3S_2@MWCNTs electrode is suggested to originate from its high active surface area and co-catalyst materials of Ni_3S_2 and MWCNTs.

The active area of each CE was evaluated by the CV technique at different scan rates, based on $K_3Fe(CN)_6$ and KCl electrolytes. The CV curves of Ni_3S_2 and co-catalyst Ni_3S_2@MWCNTs CEs are illustrated in Fig. 5 (a) and (b), respectively. It can be seen that the current of oxidation and reduction peaks increases with the increase of scan rate. These redox currents of $[Fe(CN)_6]^{3-/4-}$ (I_p) vs the square root of the scan rate ($\nu^{1/2}$) curves of CEs are shown in Fig. 5 (c). In the Randles–Sevcik equation (6), the slope of $|I_p\text{-}\upsilon^{1/2}|$ curve is proportionally related to the active surface area as described in literature [43,44]. According to this equation, the values of n, D and C are kept constant for all samples. The

Table 1
Summary of series resistance (R_s), charge-transfer resistance at counter electrode/electrolyte (R_{ct}), slope of the oxidation and reduction of I_p-$\upsilon^{1/2}$ curves of MWCNTs, Ni_3S_2 and co-catalyst Ni_3S_2@MWCNTs $_2$ CEs.

Counter electrode	EIS				Slope ($mAs^{1/2}V^{-1/2}$)	
	R_S (Ω)	R_{ct} (Ω)	R_D (Ω)	C_μ (μF)	oxidation	reduction
MWCNTs	15.20	262.62	23.14	0.39	0.31	−0.25
Ni_3S_2	15.61	16.50	5.34	1.68	0.43	−0.31
Ni_3S_2@MWCNTs	16.02	7.25	3.07	2.26	0.52	−0.38
Pt	13.56	22.31	3.13	2.09	–	–

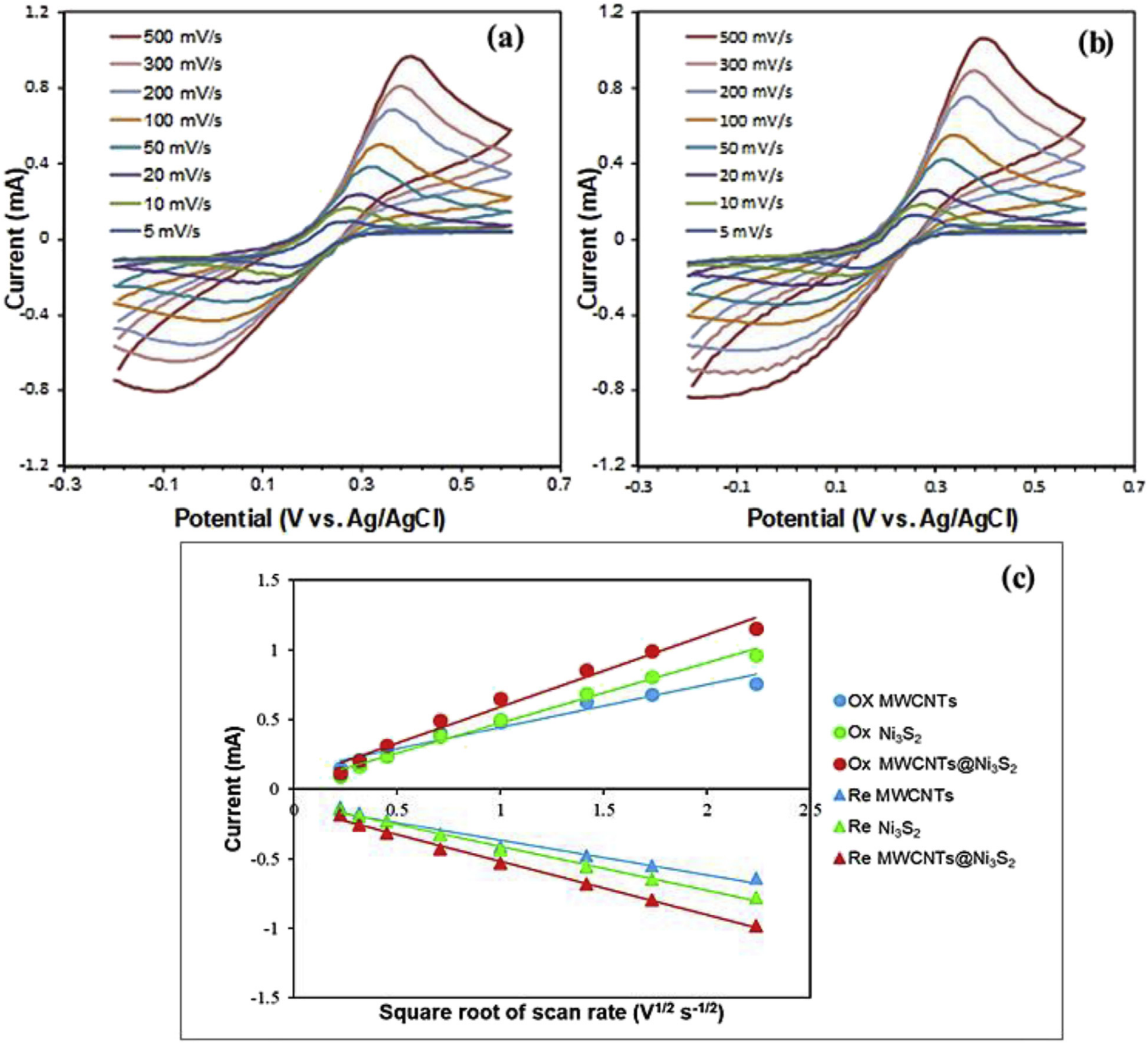

Fig. 5. CV curves of CEs at different scan rates in a mixed solution of 10 mM $K_3(FeCN)_6$ and 0.1 M KCl (a) Ni_3S_2 film, (b) co-catalyst Ni_3S_2@MWCNTs film and (c) plots of the oxidation and reduction currents of $[Fe(CN)_6]^{4-}$ (I_p) vs $\nu^{1/2}$ with their corresponding fittings.

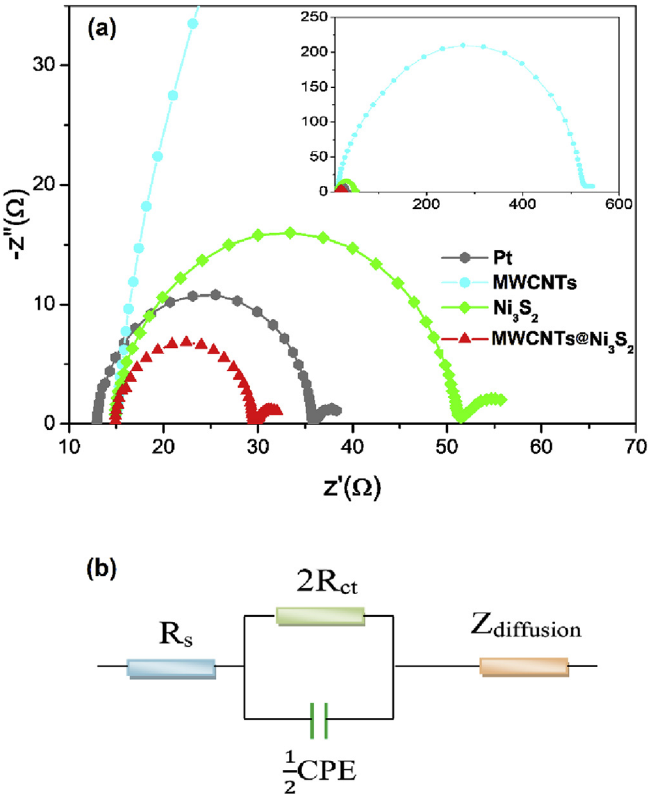

Fig. 6. (a) Nyquist plots of symmetrical cells of Ni_3S_2 and co-catalyst Ni_3S_2@MWCNTs CEs and (b) schematic representation of CE-CE equivalent circuit.

enhancements of I_p-$\upsilon^{1/2}$ slopes of the Ni_3S_2@MWCNTs CEs indicate the evolution of the surface area.

$$I_p = 2.65 \times 10^5 n^{3/2} A D^{1/2} C \upsilon^{1/2}, \qquad (6)$$

where I_p is the peak current, n is the number of electrons in the reaction, A is the electrode area (cm^2), D is the diffusion coefficient of the species of interest (cm^{2}s^{-1}), C is the concentration of the species in the bulk solution (mol·L^{-1}) and ν is the scan rate (mV/s). Values of the fitted slopes are summarized in Table 1. The absolute reduction and oxidation slopes of the Ni_3S_2@MWCNTs CE are higher than those of pure MWCNTs and Ni_3S_2 CEs. This indicates that the effective surface area of co-catalyst Ni_3S_2@MWCNTs materials is significantly improved. In general, a large surface area is important for CE, because it can raise the possibility of the triiodide reaction.

To study the internal charge transfer of these CEs, the EIS was performed to analyze the symmetrical CE (CE-CE) cells under dark condition at the AC- current amplitude of 10 mV with a frequency ranging from 0.1 Hz to 100 kHz, and all the EIS spectra of these CEs are presented in Fig. 6 (a). As seen in Fig. 6 (a), each sample reveals two semicircles curve, for which the data are fitted by using Gamry Echem Analyst software in accordance with the equivalent circuit shown in Fig. 6 (b). The equivalent circuit consists of a serie resistance (R_s), an interface charge-transfer resistance (R_{ct}) of the CE/electrolyte, corresponding to the first semicircle in the high frequency region, a constant phase element and a second semicircle in the low frequency region represents the Nernst diffusion impedance (Z_N) of an ion in electrolyte. The obtained EIS values are listed in Table 1. The first parameter R_{ct} relates to the electron transfer during the redox reaction at CE surface between I_3^- and CE. The R_{ct} values can be estimated from the real part of the first semicircle curve. As seen in Fig. 6 (a) and Table 1, the R_{ct} value reduces from 16.50 to 7.25 Ω with the MWCNTs loading. Generally, low resistance implies a higher electron transfer rate, leading to the greater power conversion efficiency. This means that the co-catalyst Ni_3S_2@MWCNTs CE has a faster electron transport with an excellent electrocatalytic activity for the triiodide electrochemical reaction. Furthermore, the Nernst diffusion resistances (R_D) were calculated from porous bounded Warburg element shown in equation (7).

$$R_D = \frac{B}{Y} \qquad (7)$$

where Y is the magnitude of the admittance at ω = 1 rad/s, and B is the characterized time taken for a reactant to diffuse through a thin film [45]. R_D represent the electron diffusion across the porous of thin film counter electrode in a redox medium. The increasing of diffusion coefficients can be considered from the Nernst diffusion resistances (R_D). Generally, the low R_D represents a high diffusion rate of ions in electrolyte. The Ni_3S_2@MWCNTs counter electrode displayed the lowest R_D, implying the highest diffusion coefficients. At the surface of counter electrode, the triiodide receives electron and becomes iodide ($I_3^- + 2e^- = 3I^-$). The increasing of iodide concentrations from this reduction process could enhance the ion diffusion coefficient in a redox mediate. This because synergetic effect of co-electrocatalyste materials (Ni_3S_2 and MWCNTs) help improve the electro catalytic activity. Low R_D implies a high tri-iodide/iodide transport. The Ni_3S_2@MWCNTs CE shows a low R_D of 3.07 Ω. In addition, the double-layer capacitance (C_μ) values are correlated with the effective surface area of counter electrodes. High capacitance implies a large effective surface area as well [46,47]. Principally, C_μ can be described by a constant phase element of impedance (Z_{CPE}) in equation (8),

$$Z_{CPE} = \frac{1}{(j\omega)^\alpha Y_0} \qquad (8)$$

where ω is the angular frequency, Y_0 is the CPE parameter or C_μ, and α is the CPE exponent (0 ≤ α ≤ 1). The C_μ value of Ni_3S_2@MWCNTs, MWCNTs, Ni_3S_2 and Pt CEs were determined and found to be 2.26, 0.39, 1.68 and 2.09 μF, respectively. Consequently, it is suggested that the Ni_3S_2@MWCNTs CE has the largest effective surface area.

The power conversion efficiency of DSSCs was measured by a solar simulator system (Peccell, PE-L111, Japan) at AM 1.5. Fig. 7 displays the J-V curves of these DSSCs based on CEs made of MWCNTs (MWCNTs-DSSC), Ni_3S_2 (Ni_3S_2-DSSC) and co-catalyst Ni_3S_2@MWCNTs (MWCNTs- Ni_3S_2-DSSC). The energy conversion efficiency (η) and fill factor (FF) of these solar cells were calculated using equations (9) and (10), respectively.

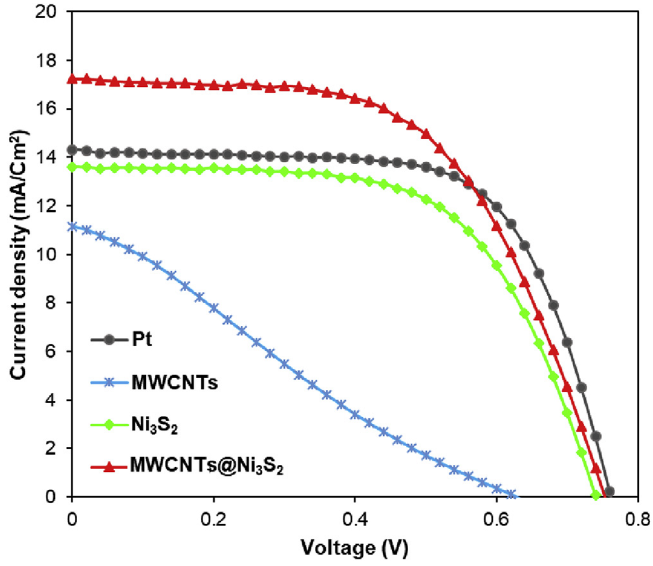

Fig. 7. Plots of photocurrent density (J) as a function of voltage (V) for DSSCs based on MWCNTs, Ni_3S_2, co-catalyst Ni_3S_2@MWCNTs and Pt CEs.

Table 2
Photovoltaic characteristics of DSSCs based on MWCNTs, Ni_3S_2, co-catalyst Ni_3S_2@MWCNTs and Pt CEs; open circuit voltage (V_{oc}), short circuit current density (J_{sc}), Fill factor (FF) and solar cell efficiency (η).

Counter electrode	J-V			
	J_{sc} (mA/cm^2)	V_{oc} (V)	FF	η (%)
Pt	14.33	0.76	0.65	7.24
MWCNTs	11.14	0.63	0.24	1.66
Ni_3S_2	13.61	0.74	0.61	6.21
Ni_3S_2@MWCNTs	17.25	0.75	0.56	7.48

$$\eta = \frac{FF.\, J_{sc}.\, V_{oc}}{P_{light}} 100\% \tag{9}$$

$$FF = \frac{J_{max}.\, V_{max}}{J_{sc}.\, V_{oc}} \tag{10}$$

Photovoltaic parameters were determined from the J-V curves and the obtained values are summarized in Table 2. From these data, it can be seen that the NiS-DSSC yields a short circuit current density (J_{sc}) of 13.61 mA/cm^2 and the open-circuit voltage (V_{oc}) of 0.74 V, which are less than the J_{sc} (17.25 mA/cm^2) and V_{oc} (0.75 V) of Ni_3S_2@MWCNTs -DSSC. The increase of J_{sc} results in the enhancement of a solar cell performance based on Ni_3S_2@MWCNTs CE (7.48%), which is higher than those of the Ni_3S_2-DSSC (6.21%) and Pt-DSSC (7.24%). The enhancement of cell efficiency in Ni_3S_2@MWCNTs -DSSC mainly arises from the raise in active surface area of CE, supporting the electrochemical activity of electrode, as confirmed by the increase of the CV slope (shown in Fig. 3 (c)) and co-catalyst Ni_3S_2@MWCNTs materials. As seen in Table 2, MWCNTs-DSSC yields the lowest value of FF (0.24), J_{sc} (11.14 mA/cm^2) and performance (1.66%), which is probably due to the small amount of MWCNTs loading. Moreover, the poor FF of MWCNTs-DSSC indicates a large internal resistance of DSSC.

4. Conclusion

The hydrothermal method can be successfully employed to prepare the composite Ni_3S_2 NPs/MWCNTs on the conducting glass substrate (FTO) to promote the improvement of the effective surface area of the CE for the high efficiency DSSC. Furthermore, the co-catalyst Ni_3S_2@ MWCNTs film can enhance the iodide/triiodide redox activity and result in the improvement of a solar cell performance from 6.21% in Ni_3S_2-DSSC to 7.48% in MWCNTs-NiS-DSSC. The enhancement of solar cell efficiency is suggested to originate from the increase of the effective surface area of the CE and the reduction of the R_{ct}. Moreover, it is suggested that the composite Ni_3S_2@MWCNTs film may be applicable for an electrode of supercapacitor as well.

Acknowledgements

This work was supported by the Thailand Research Fund (TRF), The Office of the Higher Education Commission (OHEC) (MRG6180267); Thailand Toray Science Foundation (TTSF); The Post-doctoral Program from Research Affairs and Graduate School, Khon Kaen University (Grant no. 58227); the Research Network NANOTEC (RNN) program of the National Nanotechnology Center (NANOTEC), NSTDA, Ministry of Higher Education, Science, Research and Innovation and Khon Kaen University, Thailand; and This research was supported by Mahasarakham University in 2020 and partially supported by Faculty of Science, Mahasarakham University, Thailand.

Appendix A. Supplementary data

Supplementary data to this article can be found online at https://doi.org/10.1016/j.cap.2019.08.020.

References

[1] B. O'Regan, M. Grätzel, A low-cost, high-efficiency solar cell based on dye-sensitized colloidal TiO2 films, Nature 353 (1991) 737–740.

[2] W.J. Lee, E. Ramasamy, D.Y. Lee, J.S. Song, Performance variation of carbon counter electrode based dye-sensitized solar cell, Sol. Energy Mater. Sol. Cells 92 (2008) 814–818.

[3] B. Munkhbayar, S. Hwang, J. Kim, K. Bae, M. Ji, H. Chung, H. Jeong, Photovoltaic performance of dye-sensitized solar cells with various MWCNT counter electrode structures produced by different coating methods, Electrochim. Acta 80 (2012) 100–107.

[4] R. Kumar, S.S. Nemala, S. Mallick, P. Bhargava, Synthesis and characterization of carbon based counter electrode for dye sensitized solar cells (DSSCs) using sugar free as a carbon material, Sol. Energy 144 (2017) 215–220, https://doi.org/10.1016/j.solener.2017.01.030.

[5] J. Ma, W. Shen, C. Li, J. Zheng, F. Yu, Graphene cryogel-based counter electrode materials freeze-dried using different solution media for dye-sensitized solar cells, Chem. Eng. J. 319 (2017) 155–162, https://doi.org/10.1016/j.cej.2017.03.010.

[6] Q. Qin, J. Tao, Y. Yang, Preparation and characterization of polyaniline film on stainless steel by electrochemical polymerization as a counter electrode of DSSC, Synth. Met. 160 (2010) 1167–1172.

[7] J. Wu, Q. Li, L. Fan, Z. Lan, P. Li, J. Lin, S. Hao, High-performance polypyrrole nanoparticles counter electrode for dye-sensitized solar cells, J. Power Sources 181 (2008) 172–176.

[8] J.G. Chen, H.Y. Wei, K.C. Ho, Using modified poly(3,4-ethylene dioxythiophene): poly(styrene sulfonate) film as a counter electrode in dye-sensitized solar cells, Sol. Energy Mater. Sol. Cells 91 (2007) 1472–1477.

[9] S.S. Nemala, P. Kartikay, R.K. Agrawal, P. Bhargava, S. Mallick, S. Bohm, Few layers graphene based conductive composite inks for Pt free stainless steel counter electrodes for DSSC, Sol. Energy 169 (2018) 67–74 https://doi.org/10.1016/j.solener.2018.02.061.

[10] S. Widodo, G. Wiranto, M.N. Hidayat, Fabrication of dye sensitized solar cells with spray coated carbon nano tube (CNT) based counter electrodes, Energy Procedia 68 (2015) 37–44 https://doi.org/10.1016/j.egypro.2015.03.230.

[11] L. Zheng, C. Bao, S. Lei, J. Wang, F. Li, P. Sun, N. Huang, L. Fang, X. Sun, In situ growing CNTs encapsulating nickel compounds on Ni foils with ethanol flame method as superior counter electrodes of dye-sensitized solar cells, Carbon N. Y. 133 (2018) 423–434 https://doi.org/10.1016/j.carbon.2018.03.062.

[12] L. Chen, H. Dai, Y. Zhou, Y. Hu, T. Yu, J. Liu, Z. Zou, Porous , single crystalline titanium nitride nanoplates grown on carbon Fibers ouan excellent counter electrode for low-cost , high performance , fiber-shaped dye-sensitized solar cells, Chem. Commun. 50 (2014) 1–16 https://doi.org/10.1039/C4CC03882G.

[13] M. Wu, Q. Zhang, J. Xiao, C. Ma, X. Lin, C. Miao, Y. He, Y. Gao, A. Hagfeldt, T. Ma, Two flexible counter electrodes based on molybdenum and tungsten nitrides for dye-sensitized solar cells, J. Mater. Chem. 21 (2011) 10761.

[14] H. Sun, D. Qin, S. Huang, X. Guo, D. Li, Y. Luo, Q. Meng, Dye-sensitized solar cells with NiS counter electrodes electrodeposited by a potential reversal technique, Energy Environ. Sci. 4 (2011) 2630.

[15] H.K. Mulmudi, S.K. Batabyal, M. Rao, R.R. Prabhakar, N. Mathews, Y.M. Lam, S.G. Mhaisalkar, Solution processed transition metal sulfides: application as counter electrodes in dye sensitized solar cells (DSCs), Phys. Chem. Chem. Phys. 13 (2011) 19307–19309, https://doi.org/10.1039/C1CP22817J.

[16] J. Huo, M. Zheng, Y. Tu, J. Wu, L. Hu, S. Dai, A high performance cobalt sulfide counter electrode for dye-sensitized solar cells, Electrochim. Acta 159 (2015) 166–173.

[17] M. Wu, X. Lin, Y. Wang, L. Wang, W. Guo, D. Qi, X. Peng, A. Hagfeldt, M. Grätzel, T. Ma, Economical Pt-free catalysts for counter electrodes of dye-sensitized solar cells, J. Am. Chem. Soc. 134 (2012) 3419–3428, https://doi.org/10.1021/ja209657v.

[18] J.S. Jang, D.J. Ham, E. Ramasamy, J. Lee, J.S. Lee, Platinum-free tungsten carbides as an efficient counter electrode for dye sensitized solar cells, Chem. Commun. 46 (2010) 8600–8602, https://doi.org/10.1039/C0CC02247K.

[19] S. Yun, L. Wang, C. Zhao, Y. Wang, T. Ma, A new type of low-cost counter electrode catalyst based on platinum nanoparticles loaded onto silicon carbide (Pt/SiC) for dye-sensitized solar cells, Phys. Chem. Chem. Phys. 15 (2013) 4286–4290, https://doi.org/10.1039/C3CP44048F.

[20] F. Gong, X. Xu, Z. Li, G. Zhou, Z.-S. Wang, NiSe2 as an efficient electrocatalyst for a Pt-free counter electrode of dye-sensitized solar cells, Chem. Commun. 49 (2013) 1437–1439, https://doi.org/10.1039/C2CC38621F.

[21] Z. Zhang, S. Pang, H. Xu, Z. Yang, X. Zhang, Z. Liu, X. Wang, X. Zhou, S. Dong, X. Chen, L. Gu, G. Cui, Electrodeposition of nanostructured cobalt selenide films towards high performance counter electrodes in dye-sensitized solar cells, RSC Adv. 3 (2013) 16528–16533, https://doi.org/10.1039/C3RA42360C.

[22] W. M, S. P, M. T, P. R, S. L, W. J, V. Amornkitbamrung, Co-electrophoretic deposition multiwall carbon nanotubes/Pt counter electrodes for dye-sensitized solar cell, Jpn. J. Appl. Phys. 51 (2012) 10NE20 http://stacks.iop.org/1347-4065/51/i=10S/a=10NE20.

[23] G. Yue, J. Wu, J.-Y. Lin, Y. Xiao, S.-Y. Tai, J. Lin, M. Huang, Z. Lan, A counter electrode of multi-wall carbon nanotubes decorated with tungsten sulfide used in dye-sensitized solar cells, Carbon N. Y. 55 (2013) 1–9, https://doi.org/10.1016/j.carbon.2012.10.045.

[24] G. Li, F. Wang, Q. Jiang, X. Gao, P. Shen, Carbon nanotubes with titanium nitride as a low-cost counter-electrode material for dye-sensitized solar cells, Angew. Chem. Int. Ed. 49 (2010) 3653–3656, https://doi.org/10.1002/anie.201000659.

[25] R. Bajpai, S. Roy, P. Kumar, P. Bajpai, N. Kulshrestha, J. Rafiee, N. Koratkar,

D.S. Misra, Graphene supported platinum nanoparticle counter-electrode for enhanced performance of dye-sensitized solar cells, ACS Appl. Mater. Interfaces 3 (2011) 3884–3889, https://doi.org/10.1021/am200721x.

[26] J. Ma, W. Shen, F. Yu, Graphene-enhanced three-dimensional structures of MoS 2 nanosheets as a counter electrode for Pt-free efficient dye-sensitized solar cells, J. Power Sources 351 (2017) 58–66, https://doi.org/10.1016/j.jpowsour.2017.03.047.

[27] B. Kilic, S. Turkdogan, O.C. Ozer, M. Asgin, O. Bayrakli, G. Surucu, A. Astam, D. Ekinci, Produce of graphene/iron pyrite (FeS2) thin films counter electrode for dye-sensitized solar cell, Mater. Lett. 185 (2016) 584–587, https://doi.org/10.1016/j.matlet.2016.06.069.

[28] Y. Xiao, J. Wu, J. Lin, G. Yue, J. Lin, M. Huang, Y. Huang, Z. Lan, L. Fan, A high performance Pt-free counter electrode of nickel sulfide/multi-wall carbon nanotube/titanium used in dye-sensitized solar cells, J. Mater. Chem. A. 1 (2013) 13885–13889, https://doi.org/10.1039/C3TA12972A.

[30] R. Zhang, C. Lu, Z. Shi, T. Liu, T. Zhai, W. Zhou, Hexagonal phase NiS octahedrons co-modified by 0D-, 1D-, and 2D carbon materials for high-performance supercapacitor, Electrochim. Acta 311 (2019) 83–91 https://doi.org/10.1016/j.electacta.2019.04.111.

[31] L.-X. Yang, Y.-J. Zhu, H. Tong, Z.-H. Liang, L. Li, L. Zhang, Hydrothermal synthesis of nickel hydroxide nanostructures in mixed solvents of water and alcohol, J. Solid State Chem. 180 (2007) 2095–2101 https://doi.org/10.1016/j.jssc.2007.05.009.

[32] M. Abdullah, S.K. Kamarudin, L.K. Shyuan, TiO2 nanotube-carbon (TNT-C) as support for Pt-based catalyst for high methanol oxidation reaction in direct methanol fuel cell, Nanoscale Res. Lett. 11 (2016) 553, https://doi.org/10.1186/s11671-016-1587-2.

[33] J.K. Kibet, B.C. Mosonik, V.O. Nyamori, S.M. Ngari, Free radicals and ultrafine particulate emissions from the co-pyrolysis of Croton megalocarpus biodiesel and fossil diesel, Chem. Cent. J. 12 (2018) 89, https://doi.org/10.1186/s13065-018-0458-6.

[34] Y.R. Lee, S.C. Kim, H. Lee, H.M. Jeong, A. V Raghu, K.R. Reddy, B.K. Kim, Graphite oxides as effective fire retardants of epoxy resin, Macromol. Res. 19 (2011) 66–71, https://doi.org/10.1007/s13233-011-0106-7.

[35] S. Bai, K. Zhang, L. Wang, J. Sun, R. Luo, D. Li, A. Chen, Synthesis mechanism and gas-sensing application of nanosheet-assembled tungsten oxide microspheres, J. Mater. Chem. A. 2 (2014) 7927–7934, https://doi.org/10.1039/C4TA00053F.

[36] A.A. Shamsuri, R. Daik, Utilization of an ionic liquid/urea mixture as a physical coupling agent for agarose/talc composite films, Materials 6 (2013) 682–698, https://doi.org/10.3390/ma6020682.

[37] C.N.R. Rao, R. Venkataraghavan, T.R. Kasturi, Contribution to the infrared spectra OF ORGANOSULPHUR compounds, Can. J. Chem. 42 (1964) 36–42, https://doi.org/10.1139/v64-006.

[38] A. Molla, M. Sahu, S. Hussain, Synthesis of tunable band gap semiconductor nickel sulphide nanoparticles: rapid and round the clock degradation of organic dyes, Sci. Rep. 6 (2016) 26034 https://doi.org/10.1038/srep26034.

[39] Y. Nishikitani, T. Kubo, T. Asano, Modeling of photocurrent in dye-sensitized solar cells fabricated with PVDF-HFP-based gel-type polymeric solid electrolyte, Compt. Rendus Chem. 9 (2006) 631–638, https://doi.org/10.1016/j.crci.2005.02.045.

[40] E. Ramasamy, J. Lee, Ferrocene-derivatized ordered mesoporous carbon as high performance counter electrodes for dye-sensitized solar cells, Carbon N. Y. 48 (2010) 3715–3720 https://doi.org/10.1016/j.carbon.2010.06.033.

[41] A. Hilmi, T.A. Shoker, T.H. Ghaddar, Universal low-temperature MWCNT-COOH-based counter electrode and a new thiolate/disulfide electrolyte system for dye-sensitized solar cells, ACS Appl. Mater. Interfaces 6 (2014) 8744–8753, https://doi.org/10.1021/am501520s.

[42] W. Maiaugree, S. Lowpa, M. Towannang, P. Rutphonsan, A. Tangtrakarn, S. Pimanpang, P. Maiaugree, N. Ratchapolthavisin, W. Sang-aroon, W. Jarernboon, V. Amornkitbamrung, A dye sensitized solar cell using natural counter electrode and natural dye derived from mangosteen peel waste, Sci. Rep. 5 (2015) 15230 https://doi.org/10.1038/srep15230.

[43] N. Punbusayakul, S. Talapatra, L. Ci, W. Surareungchai, P.M. Ajayan, Double-walled carbon nanotube electrodes for electrochemical sensing, Electrochem. Solid State Lett. 10 (2007) F13–F17.

[44] W. Maiaugree, S. Pimanpang, M. Towannang, S. Saekow, W. Jarernboon, V. Amornkitbamrung, Optimization of TiO2 nanoparticle mixed PEDOT–PSS counter electrodes for high efficiency dye sensitized solar cell, J. Non-Cryst. Solids 358 (2012) 2489–2495, https://doi.org/10.1016/j.jnoncrysol.2011.12.104.

[45] F. Zhang, M.D. Merrill, J.C. Tokash, T. Saito, S. Cheng, M.A. Hickner, B.E. Logan, Mesh optimization for microbial fuel cell cathodes constructed around stainless steel mesh current collectors, J. Power Sources 196 (2011) 1097–1102 https://doi.org/10.1016/j.jpowsour.2010.08.011.

[46] X. Lin, M. Wu, Y. Wang, A. Hagfeldt, T. Ma, Novel counter electrode catalysts of niobium oxides supersede Pt for dye-sensitized solar cells, Chem. Commun. 47 (2011) 11489–11491.

[47] M. Wu, X. Lin, A. Hagfeldt, T. Ma, A novel catalyst of WO2 nanorod for the counter electrode of dye-sensitized solar cells, Chem. Commun. 47 (2011) 4535–4537, https://doi.org/10.1039/c1cc10638d.